CHALMERS
UNIVERSITY OF TECHNOLOGY

Characterization of the 3D nanostructure of amorphous solid dispersions

Master's thesis in Applied Physics

MARTINA OLSSON

DEPARTMENT OF PHYSICS

CHALMERS UNIVERSITY OF TECHNOLOGY
Gothenburg, Sweden 2020
www.chalmers.se

Master's thesis 2020

Characterization of the 3D nanostructure of amorphous solid dispersions

MARTINA OLSSON

CHALMERS
UNIVERSITY OF TECHNOLOGY

Department of Physics
Division of Materials Physics
Chalmers University of Technology
Gothenburg, Sweden, 2020

Characterization of the 3D nanostructure of amorphous solid dispersions
MARTINA OLSSON

Supervisors: Aleksandar Matic, Division of Materials Physics
Marianne Liebi, Division of Materials Physics

Examiner: Aleksandar Matic, Division of Materials Physics

Master's Thesis 2020

Department of Physics
Division of Materials Physics
Chalmers University of Technology
SE-412 96 Gothenburg

Pharmaceutical Technology & Development, Operations
AstraZeneca
SE-431 50 Mölndal

Characterization of the 3D nanostructure of amorphous solid dispersions
MARTINA OLSSON
Department of Physics
Chalmers University of Technology

Abstract

Dissolution enhancing formulation strategies are getting increasingly important for the pharmaceutical industry as many new upcoming drugs present a poor water solubility. A low solubility decreases the bioavailability of the drug and diminish the therapeutic effect. One method that have shown successful results of achieving increased solubility is the formulation strategy of amorphous solid dispersions which are compound that consist of an amorphous drug dispersed in a polymer carrier. Despite successful pharmaceutical compounds being produced these systems are not fully understood, and their formulation are still largely empirical. One of the key issues is to understand the morphology of the system and how it affects the pharmaceutical performance to enable a rational design process.

In this thesis the nanostructure is evaluated for a model system of amorphous solid dispersions consisting of Felodipine in ethyl cellulose. Samples were prepared through hot melt extrusion and solvent casting with drug loads between 10-80 wt% to evaluate the effect of processing method and drug load on the morphology. In addition, a partly crystalline sample of hot melt extruded 50 wt% Carbamazepine in ethyl cellulose was used as a comparison. Ptychographic X-ray nanotomography was used as the main method together with scanning calorimetry (DSC) and X-ray-scattering (SAXS/WAXS). The nanotomography resolved the three-dimensional morphology with a resolution of 100 nm and revealed a phase separation in all samples that were not detected with DSC and X-ray-scattering in the q-range accessible with a laboratory SAXS station.

The different preparation methods created different morphologies and showed that the processing method have an effect on the phase separation mechanism. The solvent casted sample revealed a morphology from phase separation through nucleation and growth while the hot melt extruded samples showed a pattern characteristic for spinodal decomposition. The drug load had a minor effect on the extent of phase separation. A low amount of crystallinity was found in all Felodipine in ethyl cellulose samples and showed that all samples remained stable in the amorphous state during storage in ambient temperature and humidity over a time period of three months. The small fraction of crystallinity that was found were detected in the drug rich phase, indicating that phase separation is an onset for crystallization.

Keywords: Amorphous solid dispersions, ptychographic X-ray nanotomography, phase separation, 3D morphology, Felodipine

Acknowledgements

First, I would like to thank my supervisors Aleksandar Matic and Marianne Liebi for their guidance and sharing their scientific competence, but also for their support and enthusiasm which have inspired me a lot. I also want to thank for the interesting discussions with AstraZeneca and a special thanks to Susanna Abrahmsén-Alami who has been my closest contact.

Furthermore, I would like to thank the many collaborators which made this thesis work possible. To start with, I want to thank the CXS group at PSI and express a special thanks to Mirko Holler and Ana Diaz for both helping me with the tomography measurements, the sample preparation and for letting me be one of the first users of the OMNY sample preparation system. I would also like to acknowledge Rydvikha Govender and Anette Larsson for helping me with the preparation of the amorphous solid dispersions. I would finally like to thank my colleagues at (K)MF, both for always being very helpful but also for the cheers and support and creating a great work atmosphere!

Finally, I would like to thank my family for the endless encouragement and support and many thanks to all my friends for five amazing years at Chalmers leading me up to this master's thesis!

Martina Olsson, Gothenburg, June 2020

Table of Contents

Introduction

One of the challenges in the pharmaceutical industry today is poor water solubility for many new drug candidates. With a low solubility the available volume of gastrointestinal fluids is incapable of dissolving the drug at a high enough rate to reach the clinical dose needed for therapeutic effect. Many new drug discovery programs show a trend toward discovering a larger ratio of drugs with higher molecular weight and hydrophobicity [1] showing the critical need for solubility enhancing techniques to improve the bioavailability of these drugs. One dissolution enhancing strategy that has proven to be successful is formulations based on amorphous solid dispersions (ASDs). An ASD consists of a drug dispersed in a stabilizing carrier matrix which often is a polymer [2].

Amorphous formulations are a common approach to improve the dissolution rate of low solubility drugs. The amorphous drug has a higher solubility due to a higher free energy relative to its crystalline counterpart. Because of the higher free energy, the amorphous state is metastable towards the crystalline state and there is a thermodynamic driving force towards crystallization. ASDs provide a strategy to stabilize the amorphous state of the drug on relevant time scales to guarantee adequate pharmaceutical performance by dispersing the drug in a polymer carrier [2].

Several pharmaceutical products on the market today are formulated as ASDs, but despite this the systems are not fully understood, and the development of formulations is largely empirical. The morphology of these compounds is still an unidentified property. Often it is simply assumed that the drug is molecularly dispersed but some studies suggest that ASDs can coexist as both nano dispersed and molecularly dispersed systems as well as being phase separated to various extents [3-6] A high miscibility between drug and polymer is important to achieve an effective ASD and more studies on how the nano- and microstructure are affecting stability and release properties are needed to enable a rational design process. In this thesis the nano- and microstructure of ASDs is investigated and related to processing methods and drug concentration.

One of the obstacles for understanding the morphology of ASDs is to find suitable characterization techniques to evaluate the nano- and microstructure. ASDs are composed of organic phases which imposes difficulties in finding a good contrast mechanism. At the same time, ASDs are sensitive to heat and radiation which present certain constraints on the characterization method. A variety of techniques have been used to study the solid-state miscibility, such as solid state nuclear magnetic resonance (ssNMR) [6], scanning electron microscopy (SEM) and transmission electron microscopy (TEM) [3], atomic force microscopy (AFM) [7], differential scanning calorimetry (DSC) [8, 9], Raman imaging [3], infrared spectroscopy (IR) [10], X-ray diffraction (XRD) [7, 11] and fluorescence spectroscopy [5, 6] However, many of these techniques suffer from limitations for evaluation of the morphology of ASDs [4]. Bulk vibrational spectroscopic techniques cannot provide size information of phase separated domains and many of the imaging spectroscopy methods lack the spatial resolution to resolve smaller domains. The techniques which offers a high spatial resolution as AFM, SEM and TEM instead lack chemical specificity [4] and are often not suitable for investigating an extended sample volume. DSC is limited in its non-isothermal nature and fluorescence spectroscopy needs the addition of fluorescent probes into the system.

A technique that have shown good results for imaging sensitive materials, such as biological and polymer samples, is ptychographic X-ray computed nanotomography (PXCT) [12-14].

PXCT is an X-ray imaging technique where a bulk sample with a size of several tens of µm is reconstructed in three dimensions with a resolution down to 10 nm [15]. The measurement can be performed under cryogenic conditions and offers a non-destructive, non-stained measurement technique. The result provides an electron density map over the full volume which enables a quantitative analysis of both size and composition of domains as well as a qualitative evaluation of the morphology in terms of connectivity, size distribution and phase separation patterns. In this thesis, ptychographic X-ray computed nanotomography is used to study the nano- and microstructure of model ASDs together with the well-established methods DSC and Small-/Wide-angle-X-ray-scattering (SAXS/WAXS).

Aim

The aim of this thesis work is to investigate the nano- and microstructure of a model system of amorphous solid dispersions and to evaluate the effect of processing methods and drug load on the morphology. The methods used are ptychographic X-ray computed nanotomography together with DSC and SAXS/WAXS. The possibility of using ptychographic X-ray computed nanotomography as a technique for investigating the nanostructure of ASDs will also be evaluated.

Theory

The amorphous state

Amorphous solids lack the three-dimensional order that exists in their crystalline counterpart and instead typically only have a short-range order (~5Å). The physical properties of the amorphous state differ from those both in the crystalline and liquid states. Structurally an amorphous solid resembles a liquid, but the mechanical properties are those of a solid. The amorphous state has gained interest in the pharmaceutical industry due to its capability of enhanced bioavailability of pharmaceutical ingredients, see further below [16].

The glass transition

Glasses are a subset of amorphous solids where the amorphous state is formed through a glass transition. A glass transition occurs if a liquid is cooled sufficiently fast so that crystallization is avoided. The crystalline state starts to be energetically favorable after the melting temperature, but a nucleation barrier needs to be passed for the atoms or molecules to start to rearrange into a crystal lattice. If the liquid is cooled sufficiently fast, the atoms or molecules do not have time to rearrange into a crystal lattice and crystallization is avoided. Eventually during the cooling process the undercooled liquid will reach a point where a drastic increase in viscosity occurs and an amorphous solid will form through the glass transition. Figure 1 shows a comparison between a system undergoing crystallization and glass transition due to different cooling rates. Crystallization is marked by a discontinuity in the thermodynamic quantities connected to the first derivative of the free energy, such as enthalpy, entropy and volume which is characteristic for a first order phase transition. The glass transition is marked by a discontinuity in the thermodynamic quantities connected to the second derivative of the free energy and is seen as a change of slope for enthalpy, entropy and volume. These changes resemble a second order phase transition, but the glass transition temperature have a weak dependence of the cooling rate and is instead referred to as a kinetic transition [17].

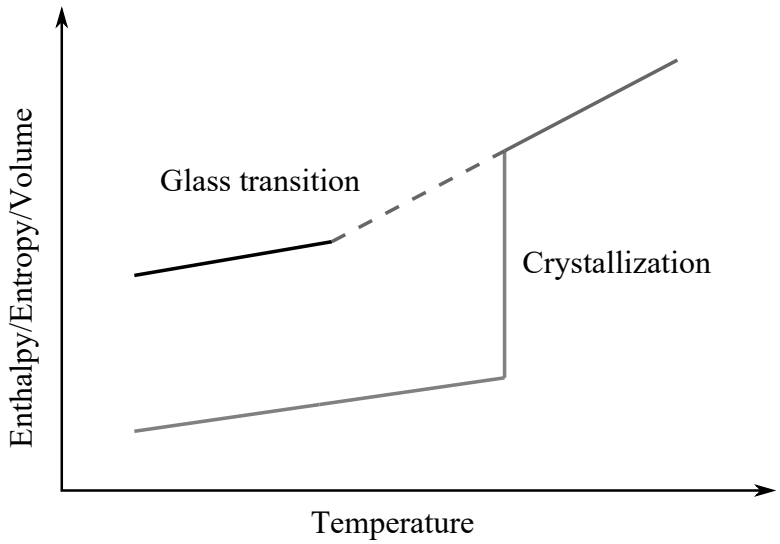

Figure 1. Schematic of a liquid undergoing crystallization and glass transition due to different cooling rates.

Increased dissolution and bioavailability of the amorphous state

The glassy state is a higher energy state than its crystalline counterpart, with a high enthalpy, entropy and volume as seen in Figure 1. Due to its higher energy, the amorphous state is

metastable, and the system will eventually crystallize. As a result of the higher energy the amorphous state has a higher solubility than its crystalline counterpart. The higher solubility depends on the lack of crystal lattice interactions or bonds that needs to be broken during dissolution. A high solubility is essential for pharmaceuticals which is why the amorphous state is of importance in the pharmaceutical industry to enhance bioavailability of poorly soluble drugs. Figure 2 shows a schematic dissolution curve for a typical amorphous and crystalline state of a poorly soluble drug. Initially the amorphous drug has a considerably higher dissolution rate than the crystalline drug but quite quickly it decreases. The decrease of solubility is due to crystallization of the drug during dissolution. To be able to utilize the higher solubility of the amorphous state in pharmaceutical compounds the amorphous state needs to be stabilized from recrystallization both during storage and dissolution. One useful technique of stabilization is to use amorphous solid dispersions which have the capability of both stabilizing the drug during storage and offer a controlled release extending the high apparent solubility during dissolution [18].

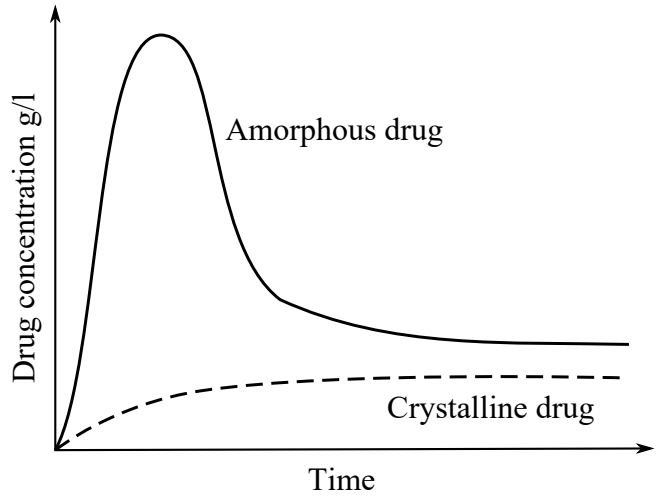

Figure 2. Schematic dissolution curve for the amorphous respectively crystalline state of drug.

Amorphous solid dispersions

Amorphous solid dispersions (ASDs) are pharmaceutical compounds designed to increase the bioavailability of poorly soluble drugs. The amorphous pharmaceutical ingredient is stabilized against crystallization by being dispersed in a carrier matrix. Usually polymers are used as carriers, and polymeric ASDs are the systems discussed in this thesis, although other carrier matrices are possible as well [2]. The amorphous state of the drug is stabilized both by increasing the kinetic barrier for crystallization and also by decreasing the thermodynamic drive towards crystallization as illustrated in Figure 3. The stabilization depends on many factors such as intermolecular interactions and an increased glass temperature in the compound. A higher glass transition temperature will decrease the molecular mobility and increase the kinetic barrier towards crystallization. Possible intermolecular interactions between the drug and the polymer, such as H-bonding, will also have an effect on the molecular mobility of the system [2, 19].

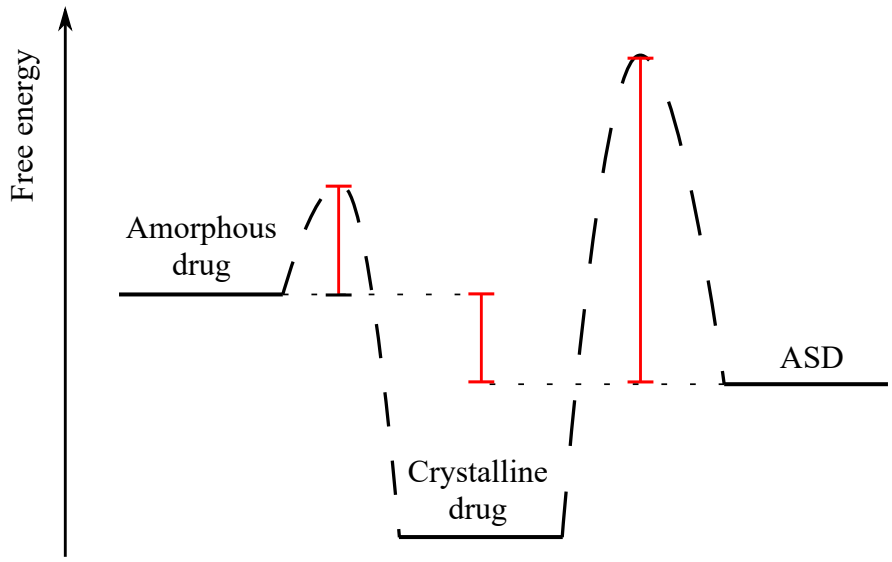

Figure 3. Schematic representation of the free energy diagram of amorphous solid dispersions showing both thermodynamically and kinetically stabilization effect on the amorphous state of the drug.

The confinement of a drug in a polymer offers several possibilities of nanostructures in the amorphous solid dispersion. The drug can be molecularly dispersed in the polymer or exist as amorphous nanoparticles [3]. The dispersion can also phase separate into larger domains of drug rich and drug poor domains [6]. A phase separation can affect the tendency to crystallize as the drug rich region can be less stable due to the lower polymer concentration. It can also affect the tendency for crystallization during dissolution [19]. The possibility of phase separation is largely affected by the miscibility between the drug and the polymer [3], [6].

Glass transition temperature of amorphous solid dispersions

When two materials with different glass transition temperatures (T_gs) are mixed together, the final T_g of the mixture will be somewhere between the T_g's of the neat materials. In the ASD the polymer is plasticized and the drug antiplasticized, resulting in a T_g intermediate of that of the neat materials [2]. If ideal mixing and volume additivity of the drug and polymer is assumed, the final T_g of the amorphous solid dispersion can be estimated with the Gordon-Taylor equation [2];

$$T_g = \frac{W_1 T_{g1} + K W_2 T_{g2}}{W_1 + K W_2} \qquad \textit{Eq. 1}$$

$$K = \frac{\rho_1 T_{g1}}{\rho_2 T_{g2}} \qquad \textit{Eq. 2}$$

where T_{g1} and T_{g2} are the individual glass transition temperatures of the drug and the polymer, W_1 and W_2 are the respective weight fractions and ρ_1 and ρ_2 are the densities of the amorphous drug and polymer [2]. The ideality of the system depends on how much the heteronuclear interactions differ from the homonuclear interactions. If the homonuclear interactions are

stronger than the heteronuclear interactions the glass transition temperatures will have a negative deviation from the theoretically estimated values [2].

Drug-polymer mixing

Miscibility between the drug and the polymer is an important property to mitigate extensive phase separation followed by crystallization and degraded performance of the amorphous solid dispersion. To quantify the miscibility in a system the free energy of mixing, ΔG_{mix}, can be examined. For a system to be miscible ΔG_{mix} has to be negative. The free energy of mixing is dependent on the enthalpy of mixing, ΔH_{mix}, and the entropy of mixing, ΔS_{mix}, as well as the temperature, T.

$$\Delta G_{mix} = \Delta H_{mix} - T\Delta S_{mix} \qquad Eq.3$$

The entropy of mixing will always be positive, meaning it will always favor mixing in the system. The enthalpy of mixing will depend on the interactions between the components in the mixture. With the use of the regular solution theory together with Flory-Huggins theory the free energy of mixing can be evaluated as;

$$\Delta G_{mix} = k_b T(\phi_D ln\phi_D + \frac{\phi_P}{p} ln\, \phi_P + \chi\phi_D\phi_P) \qquad Eq.\ 4$$

where ϕ_D and ϕ_P is the respective volume fraction of drug and polymer, p the degree of polymerization, k_b Boltzmann's constant and χ is the interaction parameter between the components. The interaction parameter is characterized as the strength of the interaction between the two components relative to their self-interactions and is also dependent on the temperature, usually promoting miscibility at higher temperatures [19].

Figure 4a show a schematic illustration of the free energy of mixing as a function of volume fraction of drug. For $\chi < 2$ the curve has a single minimum indicating full miscibility while for $\chi \geq 2$ two minima are found as illustrated in Figure 4a. The two minima mark the compositions of the coexistence curve for every interaction parameter. Outside the coexistence curve all compositions are miscible, and the mixed system is stable. Inside the coexistence curve the system is not miscible and will phase separate to reach the coexistent compositions. A phase diagram is shown in Figure 4b with the coexistence line separating the miscible and immiscible regions. The immiscible region can be divided into two parts separated by the spinodal curve. The spinodal curve is determined by the inflection point of each free energy curve (Fig. 4a). The two regions differ in the mechanism of phase separation. The region between the coexistence curve and the spinodal curve is called the metastable region because it remains stable against small fluctuations in concentration. In this region phase separation occurs by a process called nucleation and growth. The region inside the spinodal curve is called the unstable region. In the unstable region all concentration fluctuations are amplified, and a continuous phase separation takes place through spinodal decomposition [17].

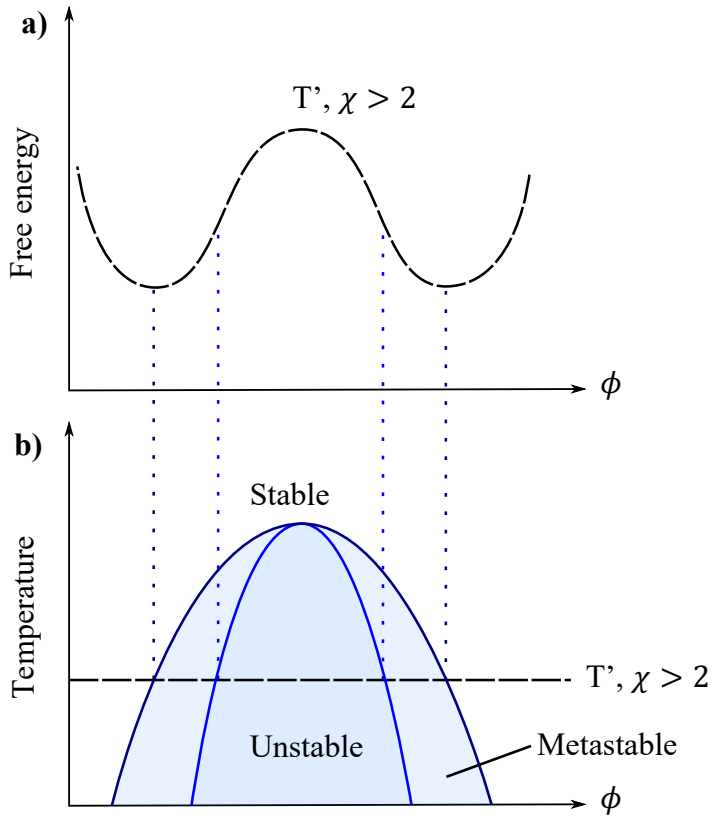

Figure 4. a) Free energy as a function of drug fraction at temperature T' with an interaction parameter $\chi > 2$. The dotted lines mark the composition at the local minima as well as the inflection points. b) The corresponding phase diagram of the drug and polymer mixture. The local minima of the free energy curve in a) mark the coexisting curve and the inflection point the spinodal line at temperature T'. These curves separate the stable, metastable and unstable regions.

Mechanisms of phase separation

Spinodal decomposition

In the unstable region, every small concentration fluctuation lowers the energy of the system resulting in a growth of all fluctuations and a continuous phase separation occurs. The reason for the continuous phase separation inside the spinodal region is due to a phenomenon called uphill diffusion where molecules diffuse from a volume of lower concentration to a volume of higher concentration. Uphill diffusion occurs because of the drive to minimize the chemical potential to reach equilibrium. In the spinodal region the chemical potential gradient has the opposite sign to the concentration gradient, leading to a diffusion of molecules from a lower concentration to a higher concentration [17].

All concentration fluctuations grow during spinodal decomposition but at different rates. Long wavelength fluctuations are slow due to the long diffusion lengths and short wavelength fluctuations cost too much energy due to the creation of a large amount of interface. An optimal size of fluctuation exists in between these two which will grow with the fastest rate. The optimal size of fluctuation generates a phase separation of domains with a characteristic length scale, but with a random pattern as illustrated in Figure 5. The characteristic length scale can be found by taking the Fourier transform of the pattern. The Fourier transformed image will show a spinodal ring where the radial average of the image has a maximum intensity at the wave vector, q_{max}, corresponding to the characteristic length scale, $l = 2\pi/q_{max}$. The Fourier transformed data can be assessed both by taking the Fourier transform of the image as well as

from scattering experiments in the far field regime which directly generate the Fourier transform of your sample [17].

Nucleation and growth

In the metastable region the mixture is stable with respect to small changes in concentration and a continuous process of phase separation will not occur. Instead a nucleus with stable composition first needs to be formed by local fluctuations. The nucleus with stable composition gives a negative contribution to the total free energy proportional to its volume and a positive contribution to the total free energy proportional to the interface created. The combined free energy contribution of a nucleus forming can be described as;

$$\Delta G(r) = \frac{4}{3}\pi r^3 \Delta G_v + 4\pi r^2 \gamma \qquad \textit{Eq. 5}$$

where r is the radius of the particle, ΔG_v the decrease in free energy per unit volume and γ the interfacial energy. The maxima of this energy curve correspond to a critical radius, r^*, of a particle for which a larger nucleus will minimize the free energy and continue to grow and create a growing phase separation [17]. Figure 5b show a schematic of a phase separation through nucleation and growth.

The process described above is known as homogenous nucleation. Another type of nucleation process is heterogenous nucleation. This occurs due to surfaces, impurities and dust present in your material that work as nucleation centers which lowers the energy required to form a nucleus and induce phase separation. In practice, heterogenous nucleation is more common [17].

After a phase separation has been induced either by spinodal decomposition or nucleation it will keep growing to minimize the energy by having lower surface energy and larger volume of coexisting phases [17].

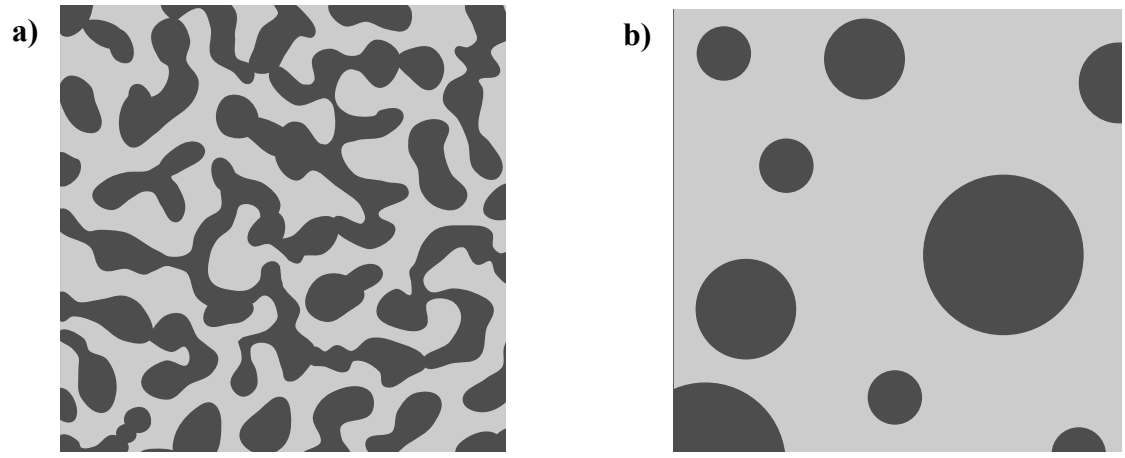

Figure 5, Schematic patterns from a) spinodal decomposition and b) nucleation and growth.

Processing methods

Various preparation methods for amorphous solid dispersions are used today, e.g. hot melt extrusion, melt granulation, solvent casting, rotary evaporation and spray drying [19]. The choice of most suitable preparation method is depending on the characteristics of your compounds such as its solubility in solvents or possible sensitivity to high temperatures. Two of the most commonly used methods are hot melt extrusion and solvent casting which are

discussed further in this section and were used as processing methods for the systems examined in this thesis work.

Hot melt extrusion

Hot melt extrusion is a common method for processing polymers in the plastic industry and is also used to produce numerous drug delivery systems [20]. During hot melt extrusion the drug and polymer are fed into a heated barrel where they are mechanically mixed during melting. The barrel contains one or two rotating screws that provide an intensive mixing of the compounds as well as providing heat by friction. After sufficient mixing the melt is extruded through a die allowing shaping of the melt directly into dosage forms [20].

A requirement for the hot melt extrusion process to be applicable is that the drug and polymer are completely miscible in the molten state. If this is fulfilled the high sheer and high temperature can provide a uniform mixture of the two components. A great advantage of hot melt extrusion is that it is a simple, continuous process with few processing steps, which makes it suitable for upscaling. It has also the advantage of being a solvent free method which eliminates problems like residual solvents and costly evaporation process steps. One of the largest disadvantages are the high temperatures needed. Both compounds need to be stable at each other's melting and softening temperatures and for the high-sheer forces during mixing which result in high local temperatures in the extruder which is a problem for heat sensitive materials [21].

Solvent casting

Solvent casting starts with preparation of a solution containing the dissolved drug and polymer followed by evaporation of the solvent leaving a solvent casted film. The dissolution in a solvent provides a molecular level mixing of the drug and polymer which is an advantage for increased stability of the product. One of the greatest advantages of solvent casting is that high temperatures are not needed for the evaporation and the risk of thermal decomposition of the compounds is avoided. Therefore, solvent casting is a good choice for heat sensitive compounds [21].

A challenge with solvent preparation methods are the choice of solvent. Both the drug and the polymer need to be soluble in the solvent which may be difficult if the compounds for instance have different polarity. Many organic solvents are hazardous and residual solvents in the product will be a problem both for safety and for stability. Another difficulty with the process is that phase separation may happen during the evaporation process. By using a higher evaporation temperature, the time for phase separation is reduced which can mitigate the process. At the same time, by increasing the temperature, the system gets a higher molecular mobility which instead can accelerate the phase separation process. In large scale production solvent preparation methods are in general expensive as evaporation and recovery of a large amount of solvent is an expensive process [21].

Characterization of amorphous solid dispersions

Differential scanning calorimetry

Differential scanning calorimetry (DSC) is a thermoanalytical method for detecting phase transitions by the response of a material during heat exposure [22]. During the measurement a sample and a reference are exposed to a heating cycle and the heat flow is measured as a function of temperature. The heat flow change is equivalent to the enthalpy change and will

show endothermic or exothermic events for phase transitions in the sample. If the sample undergoes an endothermic process the sample heat flow will be higher than the reference and vice versa for an exothermic process. The result of the measurement is given as a thermogram with the heat flow as a function of temperature. Figure 6 shows a schematic thermogram with the characteristic features of glass transition and melting events. The glass transition temperature is determined by the midpoint of the glass transition event as illustrated by a red cross in Figure 6b. The midpoint marks the maximum of the first derivative of the heat flow and this is how the glass transition temperature is determined from the thermograms in this thesis. The melting temperature is determined by the peak value of the endotherm.

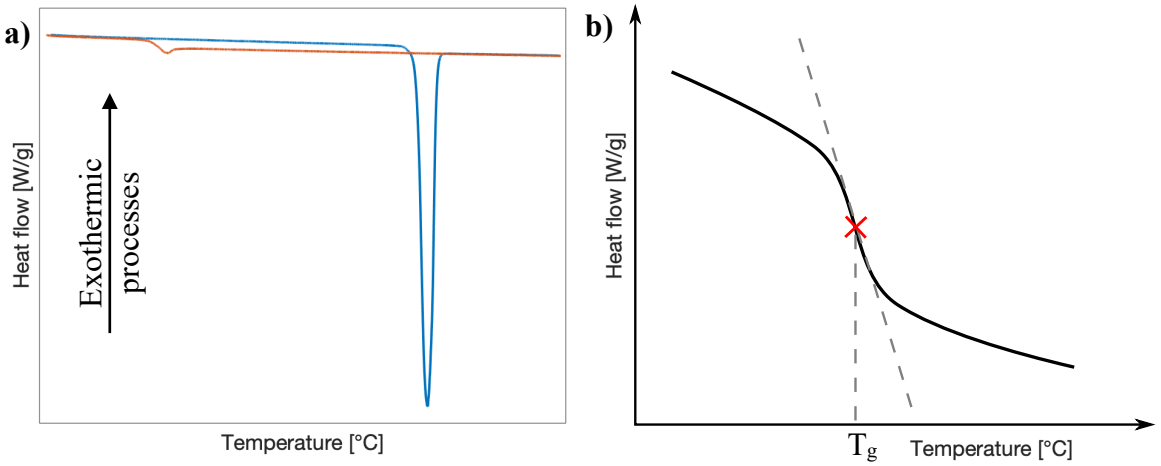

Figure 6. a) Two thermograms showing the characteristics of a glass transition (red curve) and melting (blue curve). b) Schematic illustration of how the glass transition temperature is determined at the midpoint marked with a red cross.

DSC is commonly used to detect crystallinity and investigate miscibility in amorphous solid dispersions [9]. The measurement is fast and easy but have limitations for detecting phase separation. In general, a single distinctive glass transition temperature (T_g) intermediate of the T_g's of the neat compounds is considered as characteristic of a homogenous mixed system. Since DSC is a non-isothermal technique it is important to consider the impact of increased mobility and miscibility with increased temperature during the measurement. When the temperature approaches T_g this could potentially lead to a remixing of the system and a single T_g, indicating a single uniform phase, can be detected although the ASD was phase separated before the measurement [6]. It has previously been shown that even a phase separation on the scale of tens of microns can remain undetected by DSC measurements [23].

Small-/Wide-angle-X-ray-scattering

X-ray scattering can be used to examine the nano and atomic structure of a material. By measuring the angle-dependent distribution of the scattered intensity it is possible to draw conclusion about average structures as well as morphology on the nanoscale [24].

In an X-ray scattering measurement, a sample is illuminated by a focused X-ray beam. The X-ray beam interacts with the electrons in the sample and the intensity of the scattered X-rays is recorded with a detector as a two-dimensional scattering pattern. The scattering pattern is dependent on the wavelength, λ, according to Bragg's law,

$$n\lambda = 2d \sin\theta \qquad \textit{Eq. 6}$$

where 2θ is the scattering angle, d the repeating distance and n a positive integer [24].

For convenience the scattered angles are redefined in the form of the magnitude of a scattering vector, q,

$$q = \frac{4\pi}{\lambda} \sin\theta \qquad \textit{Eq. 7}$$

The scattering vector removes the dependence on incident wavelength in the scattering pattern and simplifies the analysis between measurements from different sources. A relationship between the repeating distance, d, and the scattering vector, q, can be derived from Bragg's law and the scattering vector as $d = \frac{2\pi}{q}$ [24].

To simplify the analysis, the two-dimensional scattering pattern is usually radially averaged to a one-dimensional curve of the scattered intensity as a function of the scattering vector. For an isotropic sample the scattering will be equal in all directions in the scattering pattern and a radial averaging process will only improve the statistics. If instead the sample is partially oriented the scattering will have a preferred direction which will be seen in the 2D diffraction pattern but not in the 1D radial average [24].

The working principle for Small and Wide-angle X-ray scattering (SAXS and WAXS) are the same with the difference of the distance between the sample and the detector. The SAXS detector is further away from the sample and hence collect information of smaller angles. Smaller angles correspond to lower q-values and larger structures, often about a few nm up to a few hundred nm. A higher q-range is collected with WAXS corresponding to smaller structures in the sub-nanometer range and can give you information on crystallinity in the sample.

Ptychographic X-ray computed nanotomography

Ptychographic X-ray computed nanotomography (PXCT) is a phase-contrast imaging technique where the image is reconstructed from the far-field diffraction pattern. It is a lensless technique and the resolution is fundamentally limited by the wavelength of the X-ray beam. In practice the resolution is limited by radiation damage, mechanical instabilities and the flux, which determines the angular extent of the X-ray scattering of the sample with a sufficient signal-to-noise ratio [25]. The acieveble contrast between the phases in the sample can also be a limitation. Today's techniques enable a non-destructive, three-dimensional mapping of the interior of a bulk sample of several tens of μm with a resolution down to 10 nm [15]. By using a coherent X-ray beam together with iterative reconstruction algorithms, the technique is capable of mapping the full refractive index, including both attenuation and phase, and enables a quantitative analysis of the electron density distribution in the sample [13].

One of the advantages of X-ray imaging is the high penetration power of X-rays which offers a non-invasive imaging of the interior of bulk samples. The downside of the high energy X-rays is that the absorption contrast of the sample is low. Absorption decrease with the fourth power of the photon energy while the phase contrast scales with the inverse of the energy. This means that by being able to reconstruct the phase, it is possible to use high energy X-rays while still gaining a high contrast [13].

The PXCT technique is based on coherent diffractive imaging which uses the far-field diffraction pattern of coherent light scattering to reconstruct an image. A coherent X-ray beam has a constant phase difference between points in the coherent region over time and creates interference fringes of high contrast [26]. Coherence of the beam is needed because interference of diffracted waves is necessary for the reconstruction. The diffracted intensity is proportional to the absorption constant, but the phase information is experimentally lost as only intensities are recorded in the detector plane. This is often referred to as the phase problem. To retrieve the full refractive index certain reconstruction algorithms are needed to be able to compute it from the diffraction pattern. [27] In PXCT, the high phase sensitivity of the 2D coherent diffractive imaging is combined with computed tomography to retrieve the full 3D reconstruction.

A schematic of the setup for a PXCT measurement is seen in Figure 7. The sample is placed on a rotational stage and is illuminated by a spatially confined, coherent X-ray beam and the far-field diffraction pattern is collected for each measurement point. The sample is scanned across the beam with an overlap between measurement points. This overlap gives a redundancy in the data which makes it possible to solve the phase problem during the reconstruction of the images. To gain the full 3D reconstruction, the measurement is repeated for a chosen amount of projection angles as the sample is rotated 180 degrees. [13]

For the data processing several software processing packages have been developed [28-30]. The typical data processing starts with ptychographic reconstructions of individual projections with phase unwrapping and phase removal. The second step is to align the projections to correct for experimental inaccuracies in positioning. To obtain the tomographic reconstruction, filtered back projection (FBP) or other iterative reconstruction algorithms are computed, and a 3D reconstruction of the full refractive index is generated. Lastly, post processing steps to obtain quantitative data in the form of electron density maps is performed. [31]

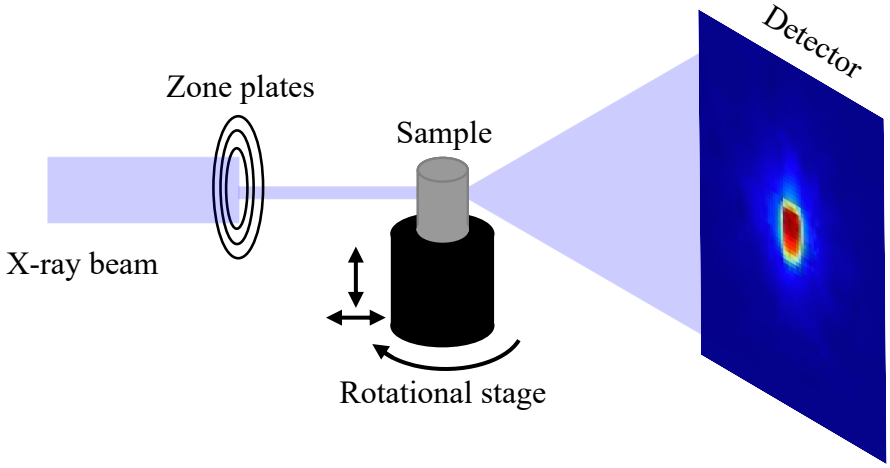

Figure 7. Schematic setup for ptychographic nanotomography. The X-ray is focused to a smaller beam by zone plates and interacts with a part of the sample. The sample is placed on a rotational, 3D piezo stage that moves the sample over the beam and the far-field diffraction pattern is collected in all measurement points.

Filtered back projection

Filtered back projection is an analytical reconstruction algorithm where the signal received through the sample is back projected along the propagation of the beam. When more and more

angles are added, the full image is reconstructed as schematically shown in Figure 8a. The back-projection alone produce blurry images and needs to be combined with a ramp filter to produce sharp images. Since the ramp filter is a high pass filter it amplifies noise, and an additional smoothing filter needs to be applied to reduce the noise and get a better reconstructed image. [32] One of the most used filters is the Ram-lak filter (Fig. 8b) which is a window function that blocks out the high-frequencies above the frequency cut-off and in that way reduce noise in the reconstruction. [33]

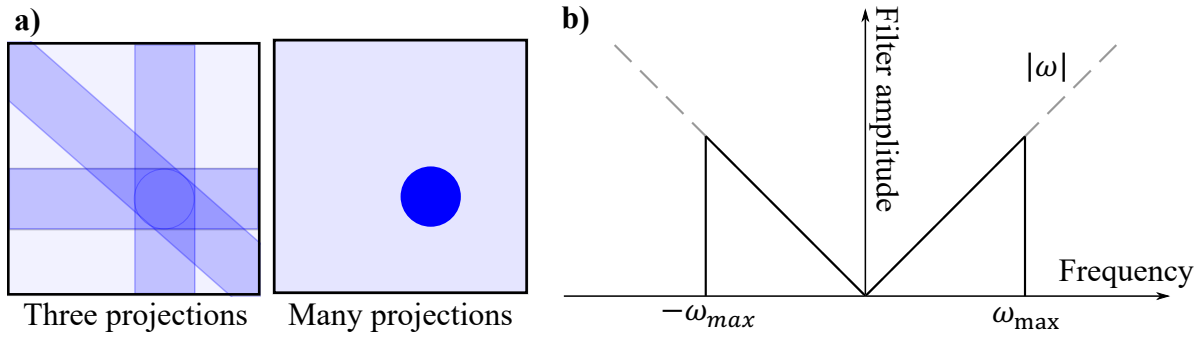

Figure 8. a) Schematic represeantation of filtered back projection reconstruction. The left image show the filtered back projection using three projection angles and the right image show the final reconstructed image that is found with many projections angles. b) A ram-lak filter with frequency cut-off ω_{max}.

Quantitative analysis

For X-ray energies far from the absorption edges the refractive index is proportional to the electron density of the sample. The formula for calculating electron density, n_e, is given by,

$$n_e(\boldsymbol{r}) = \frac{2\pi\,\delta(\boldsymbol{r})}{\lambda^2 r_0} \qquad \textit{Eq. 8}$$

where $\delta(\boldsymbol{r})$ is the 3D distribution of the refractive index, r_0 is the classical electron radius and λ the wavelength of the X-ray beam. If the chemical composition of the material is known the electron density can be related to the mass density, ρ

$$\rho(\boldsymbol{r}) = \frac{n_e(\boldsymbol{r})A}{N_A Z} \qquad \textit{Eq. 9}$$

where A is the molar mass, Z is the total number of electrons and N_A denotes Avogadros number [25, 34].

Normalized cross-correlation

Computing the correlation between two matrices, the cross correlation, is a standard approach for feature detection and determining similarity of images [35]. Normalized cross correlation (NCC) is the normalized form of cross correlation and computes a cross correlation coefficient which quantifies the correlation with a value between -1 and 1. A cross correlation coefficient of 1 denotes an exact correlation, 0 no correlation and -1 an exact negative correlation.

Normalized cross correlation is often used together with template matching which allows for finding the correct alignment of the first image on the second image while at the same time generating a quantitative value of the similarity between the two images [35]. When the two images are exactly aligned the cross-correlation coefficient will have a peak value close to 1 if the images are well correlated. Sometimes the noise and artefacts in tomograms can give a deceiving high correlation coefficient where there is no correlation [36] . The two-dimensional landscape of the correlation coefficient is a useful way to detect if these high values correspond to a real correlation or not by determining if the correlation is a peak at exact alignment. Figure 9 shows two-dimensional plots of the correlation coefficient for two identical image and for two images with a deceiving high correlation coefficient due to artefacts and noise.

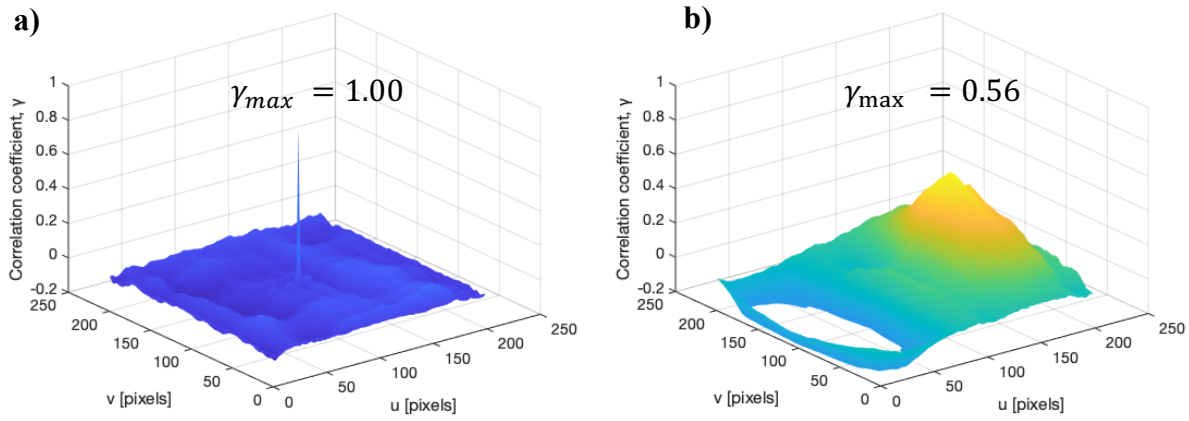

Figure 9. Schematic two-dimensional landscape of the correlation coefficient for a) two identical images and b) uncorrelated images with a deceiving high correlation coefficient due to artefacts and noise.

To compute the normalized cross correlation, the two images are denoted $f(x,y)$ and $g(x,y)$ with the size $M_x \times M_y$ where $x = [0, \dots Mx-1]$ and $y = [0, \dots Mx-1]$. The two images are compared for every pixel-wise shift of the first image with respect to the other with u discrete steps in the x direction and v steps in the y direction, and the correlation coefficient, $\gamma(u,v)$, is calculated in each position (u,v). The basic definition of the normalized correlation coefficient is,

$$\gamma(u,v) = \frac{\sum_{x,y}[f(x,y) - \bar{f}_{u,v}][g(x-u,y-v) - \bar{g})]}{\sum_{x,y}\{[f(x,y) - \bar{f}_{u,v}]^2[g(x-u,y-v) - \bar{g})]^2\}^{0.5}} \qquad \textit{Eq. 10}$$

where $\bar{f}_{u,v}$ is the mean of the first image, $f(x,y)$, within the area of the second image, $g(x,y)$, shifted to (u,v), and $\bar{g}$ is the mean of the second image. [35].

Materials

The following section describes the model drugs and polymer used in this thesis work. Felodipine and ethyl cellulose were chosen as the main model system as Felodipine is a good glass former and both compounds are relevant for pharmaceutical industries [37]. In addition, Carbamazepine in ethyl cellulose was used as a comparison due to its higher tendency to crystallize which could give a higher contrast in the nanotomography measurements. The active pharmaceutical ingredients were supplied by Astra Zeneca and ethyl cellulose (Ethocel^{TM} Standard 7 Premium) was supplied by Colorcon.

An approximate mass density of each compound is provided below and is used for correlating electron densities in the tomograms to respective compound. The mass density is dependent on processing as it is related to the molecular packing and is therefore not unambiguously determined. Because of this uncertainty, the mass densities presented here are only used as approximate references. Useful references for the density of some compounds were not found in literature and is then marked with N/A.

Felodipine

Felodipine is a calcium channel blocker and significantly reduces the blood pressure for patients with hypertension [38]**.** Figure 10 shows the molecular structure of Felodipine. Felodipine is a common model drug for amorphous solid dispersions and is a good glass former with a very poor water solubility [39]. Several polymorphs exist for crystalline Felodipine [40].

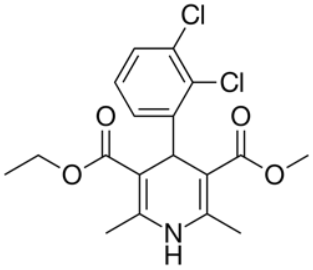

Chemical formula	$C_{18}H_{19}Cl_2NO_4$
Molecular weight [g/mol]	384.3
Melting point [°C]	147
Glass transition temp [°C]	45
Amorphous density [g/cm^3]	1.28
Crystalline density [g/cm^3]	1.42-1.45

Figure 10, Chemical structure and chemical data of Felodipine. The data is found in [37,40,56].

Carbamazepine

Carbamazepine is an antiepileptic and mood-stabilizing drug used primarily in the treatment of epilepsy and bipolar disorder [41]. Similar to Felodipine, Carbamazepine has a poor water solubility. Figure 11 shows the molecular structure of Carbamazepine. Several crystalline polymorphs exist for the drug which results in a range of densities and melting points depending on the polymorph structure [42].

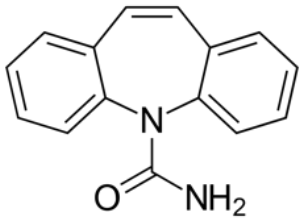

Chemical formula	$C_{15}H_{12}N_2O$
Molecular weight [g/mol]	236
Melting point [°C]	176-192
Glass transition temp [°C]	56
Amorphous density [g/cm^3]	N/A
Crystalline density [g/cm^3]	1.24-1.34

Figure 11, Chemical structure and chemical data of Carbamazepine. The data is found in [57-59].

Ethyl cellulose

Ethyl cellulose (EC) is a cellulose derivative where ethoxy groups (-OC_2H_5) have replaced some of the hydroxyl groups (-OH) on the repeating glucose units. It is used in pharmaceutical industry for controlled drug release but also for food packaging, cosmetics and coatings. [43] Figure 12 shows the molecular structure of a monomer of ethyl cellulose.

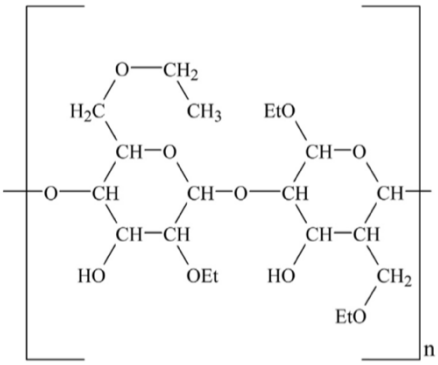

Chemical formula	$(C_{20}H_{36}O_{10})_n$
Molecular weight [g/mol]	436.5n
Glass transition temp [°C]	128-130
Amorphous density [g/cm^3]	1.14

Figure 12. Chemical structure and chemical data of ethyl cellulose. The data is found in [61].

Method

Preparation of amorphous solid dispersions

For the model system Felodipine in ethyl cellulose, both hot melt extruded strands of concentration 10, 30, 50 and 80 wt% and solvent casted films of concentration 10, 30 and 50 wt% were prepared. The highest drug load for the film were not possible to achieve as a transparent film due to crystallization during the evaporation. An example of the 30 wt% sample of respective preparation method is shown in Figure 13. In addition, hot melt extruded strands of Carbamazepine in ethyl cellulose of concentration 10, 30 and 50 wt% were prepared.

Hot melt extrusion

An Xplore Micro compounder MC 5 was used to prepare hot melt extruded samples. The temperature of the barrel was adjusted to be above the melt temperature of the drug and above the glass transition temperature of the polymer. An exception was made for the sample containing Carbamazepine and ethyl cellulose were the degradation temperature of ethyl cellulose and the melting temperature of Carbamazepine are similar. For these samples the temperature was held at T~180 °C which is lower than the melting temperature of the higher melting point polymorphs of Carbamazepine (T_m~190 °C).

A sample amount of a few grams (~5g) of drug and polymer were fed into the barrel with w/w ratio ranging from 10-80 wt% drug. The material was cycled for 10 min to ensure proper mixing of the compounds and the melt was flushed out of the extruder producing a rod like filament.

Solvent casting

Solvent casted films were prepared by dissolving the drug and polymer of choice in dichloromethane under magnetic stirring. The drug: polymer w/w ratio was varied to prepare films of different concentrations ranging from 10-50 wt% drug. The components: solvent w/v ratio used were 2-5%. After complete dissolution of the polymer and the drug in the solvent, upon visual inspection, the solution was casted onto a Teflon dish. The Teflon dish with the solution was covered with perforated parafilm to slow down evaporation and were left in a fume hood for at least 12 hours. Finally, the film was left to dry in vacuum to ensure full evaporation of dichloromethane.

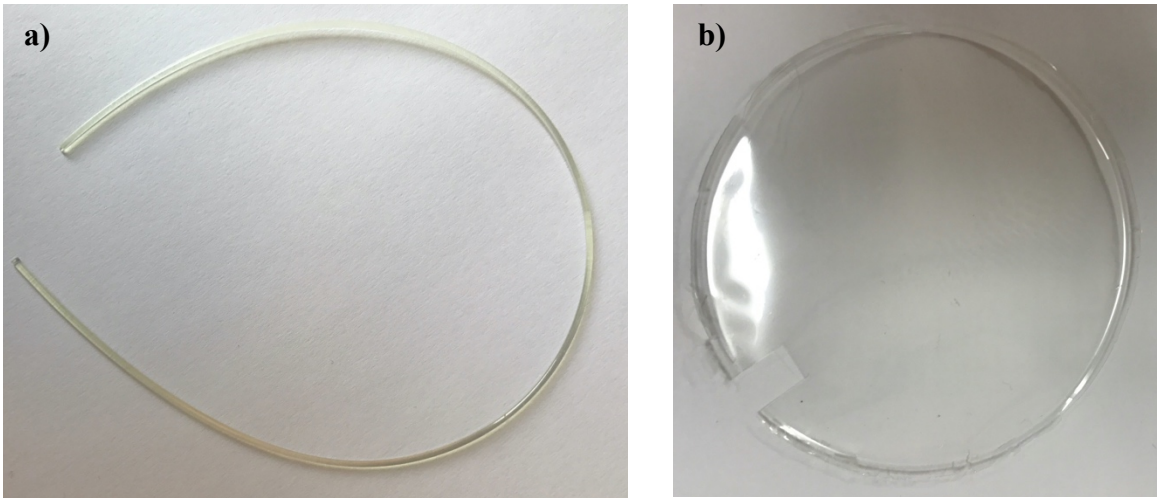

Figure 13. 30 wt% Felodipine in ethyl cellulose prepared with a) hot melt extrusion and b) solvent casting

Characterization of amorphous solid dispersions

Differential scanning calorimetry

Differential Scanning Calorimetry (DSC) measurements were carried out using a TA Q1000 instrument. A small piece of sample (~5 mg) was weighed and put in a hermetically sealed aluminum pan and an empty pan was used as reference. Helium and Nitrogen were used as purge gases for the sample chamber at a rate of 50 ml/min. All samples were put through a heating cycle with the steps of heating to 200 °C, 2 min isotherm, cooling to 0 °C, 2 min isotherm followed by a second heating step to 200 °C. The heating and cooling rates were kept at 10 °C /min.

Small-/Wide-angle X-ray-scattering

SAXS and WAXS measurements were obtained using a Mat: Nordic instrument from SAXSLAB at Chalmers Materials Analysis Laboratory (CMAL). The measurements were made through the bulk of the extruded rods and casted films. The exposure time was set to 10 min for SAXS and 5 min for WAXS to obtain good statistics. The q-ranges covered by the respective measurement were 0.4-2.2 $Å^{-1}$ and 0.006-0.25 $Å^{-1}$ corresponding to length scales of 2.5-100 nm and 0.2-1.5 nm.

Ptychographic X-ray computed nanotomography

Experimental setup

Ptychographic nanotomography measurements were performed at the cSAXS beamline of the Swiss Light Source, Paul Sherrer Institut in Switzerland. The measurements were made under cryogenic condition using the OMNY-setup. [44] The photon energy of the X-ray beam was 6.2 keV and the beam was spatially confined by zone plates and a single photon counting detector was placed 7.2 m downstream of the sample. The measuring parameters were altered during the beamtime to optimize the conditions to reach a high resolution and good statistics while minimizing radiation damage. The optimal parameters were found to be a step size of 2 µm, a counting time of 0.025 s and approximately 1600 projections. This resulted in a voxel size of 42×42 nm^2 and a resolution of about 100 nm determined by Fourier Shell correlation (FSC). FSC measures the normalized cross-correlation between two independent reconstructed volumes over corresponding shells of the sample in frequency space to determine a resolution threshold at which the reconstructions are consistent. The object is considered to be resolved up to this spatial frequency [45].

Cylindrical samples with a width of circa 50 µm were prepared for the ptychographic nanotomography experiments by mechanical milling using a lathe system under cryogenic conditions [46]. A larger piece of the sample was glued to the sample holder and were lathed to appropriate size. For samples where milling was not possible, due to material properties like brittleness or waxiness, a small µm sized piece was instead cut by hand and mounted to the sample holder [47]. Figure 14 show the lathe setup and a prepared pillar.

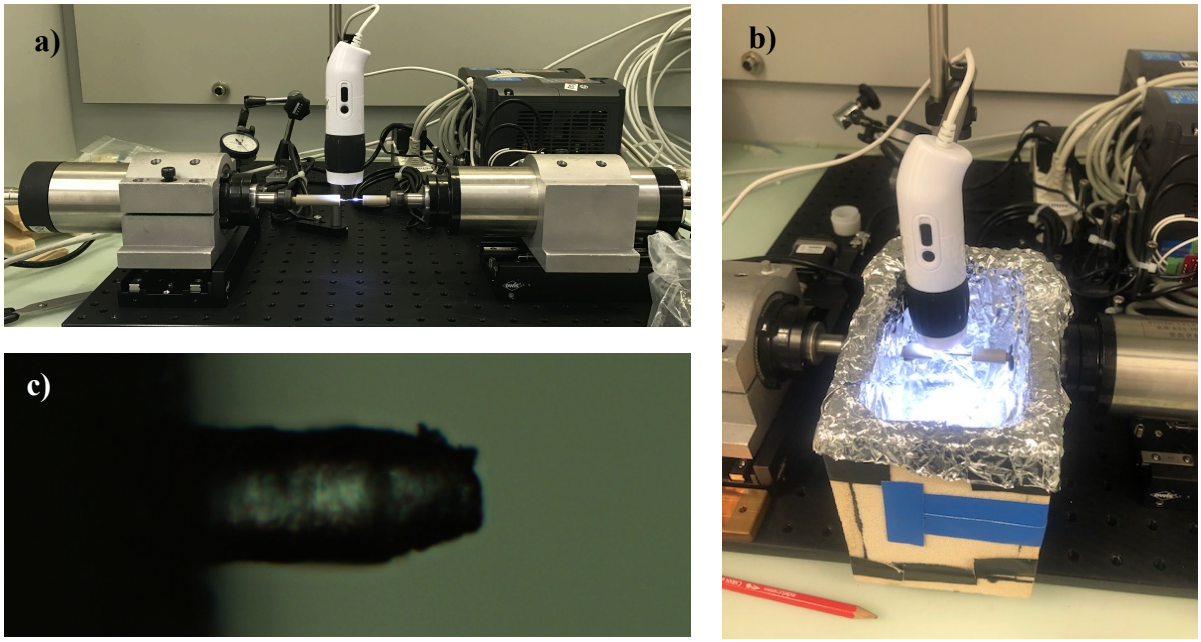

Figure 14. a) The setup of the lathe system [46] with a sample holder to the left and the drill to the right. b) The lathe system surrounded with the cryogenic chamber partly filled with liquid nitrogen and c) a prepared pillar.

Computational processing

Data processing was carried out using the "cSAXS matlab package" developed by the CXS group, Paul Scherrer Institut, Switzerland [28-30]. Alignment was made with the use of mass fluctuation and center of mass. A phase refinement was made in terms of phase ramp and phase wrap removal. Filtered back projection (FBP) was used for the reconstruction using a ram-lak filter with frequency cut-off of 1. To estimate the resolution of the tomogram, Fourier shell correlation (FSC) [45] was applied. An estimation of tomogram time evolution was made to detect changes in the sample due to radiation damage and for dividing the full data set into two individual measurements, so called sub tomograms.

Image analysis

After data processing of the ptychographic nanotomography, additional processing and image analysis followed. The image analysis can be divided into the following three steps; normalized cross correlation, filtering and morphology analysis. The following section will describe these image analysis steps.

Normalized cross-correlation

Normalized cross-correlation (NCC) were computed with the *xcorr2* implementation in MATLAB for evaluation of the accuracy of the tomograms. From two individual sub tomograms the exact same area was selected and compared. Areas were chosen of the same dimensions both in the sample as well as in the noise. The correlation coefficient was calculated for every pixel-wise shift of one image relative to the other, creating a two-dimensional landscape of the correlation coefficient.

Filtering and morphology analysis

Filtering of the images were applied to reduce noise in the tomograms. All filtering was made in FIJI [48, 49] and the result was exported for further processing in MATLAB or Avizo. A 3D mean filter with a 5×5×5-pixel kernel was applied to all hot melt extruded samples. A

background subtraction was made for the solvent casted sample using the rolling ball background subtraction to adjust for an artefact creating uneven intensity in the tomogram. In addition, a 3D mean filter with an anisotropic kernel, 5×5×9-pixels, was applied to best enhance the features in the sample. For the volume renderings a gaussian filter with a 5×5×5-pixel kernel was applied to further smooth the tomogram.

MATLAB R2019b was used to illustrate the two-dimensional electron density maps of the filtered tomogram slices and to select regions of interest. MATLAB was also used to make a quantitative analysis of the domain size and composition of phases. The domain sizes were estimated by determining an average distance between peaks of the electron densities on a profile of electron density towards distance. The estimation of the composition of the phases was made by a simple linear relationship according to

$$\rho_{mix} = x_D \rho_{eD} + (1 - x_D)\rho_{eP} \qquad \textit{Eq. 11}$$

where ρ_{mix} is the electron density of the mixed phase, ρ_{eD} and ρ_{eP} the neat electron densities of the drug and polymer and x_D the volume fraction of drug. The volume fraction is converted to mass fraction, $x_{D\,w}$, by

$$x_{D\,w} = \frac{x_D \rho_{eD}}{x_D \rho_{eD} + (1 - x_D)\rho_{eP}} \qquad \textit{Eq. 12}$$

This estimation assumes that the electron densities of the compounds are additive. The electron density of the neat drug and polymer were calculated by their theoretical mass densities with equation 9 to ρ_{eD}= 0.37 e/Å^3 and ρ_{eD}=0.40 e/Å^3. The hot melt extruded samples all have a significantly higher electron density than what would correspond to the theoretical values. For these samples the average densities of the three 10, 50 and 80 wt% were used to calculate a representation of what would likely be the neat density of the compounds to receive these averages. With this calculation the result was ρ_{eD}= 0.375 e/Å^3 and ρ_{eD}=0.415 e/Å^3. These assumptions introduce uncertainty in the determination of the compositions, and they should not be considered as an absolute value but rather as a guideline for an approximate composition.

Avizo was used to create three-dimensional renderings of the morphology as well as for segmentation of crystallinity by thresholding. From the segmentation the volume ratio of crystallinity was estimated by calculating the ratio of segmented pixels.

Result and Discussion

The following chapter describes the results from scanning calorimetry (DSC), Small-/Wide-angle-X-ray-scattering (S/WAXS) and ptychographic X-ray computed nanotomography (PXCT) measurements. The result from each individual characterization method is presented first, followed by a discussion comparing the results from the different characterization methods. Finally, the effect of processing methods and drug load on the morphology of the ASDs are discussed.

Differential scanning calorimetry

Figure 15 and 16 show the thermograms of neat Felodipine and Carbamazepine, respectively. Figure 15a and 16a show the thermograms from the first heating scan and 15b and 16b show the thermograms from the second heating scan. Both neat Felodipine and Carbamazepine are initially crystalline which can be seen by the melting endotherms in the first heating scan. Felodipine has a single melting endotherm at 145°C. Carbamazepine has a first melting endotherm at 176°C followed by an exotherm at 177°C indicating a cold crystallization and a second melting endotherm at 193°C. This thermogram indicates that the Carbamazepine was first in one polymorph, with a melting point of 176°C, and has a second polymorph with a melting temperature of 193°C.

The second heating scan shows that the Felodipine is now instead in its amorphous state and the melting endotherm is gone. Instead the thermogram shows a glass transition at 45°C. This shows that during the first heating scan the crystalline Felodipine melted and during the cooling it avoided crystallization and became a glass. The second heating scan of the Carbamazepine shows a glass transition at 45°C followed by an exotherm at 90°C indicating cold crystallization. A melting endotherm at 145°C, show that the cold crystallization generated a third polymorph.

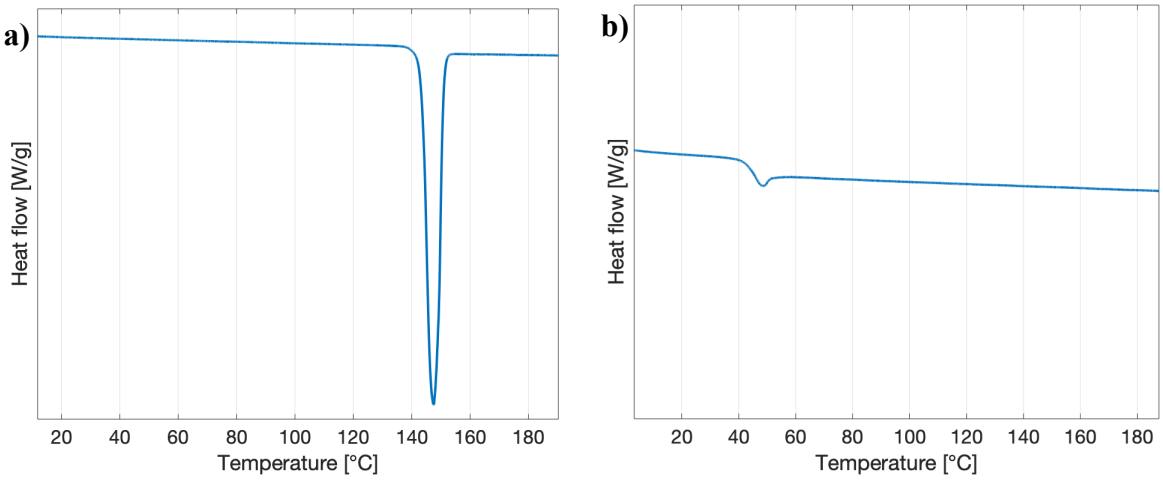

Figure 15. Thermograms of neat Felodipine from the a) first and b) second heating scans.

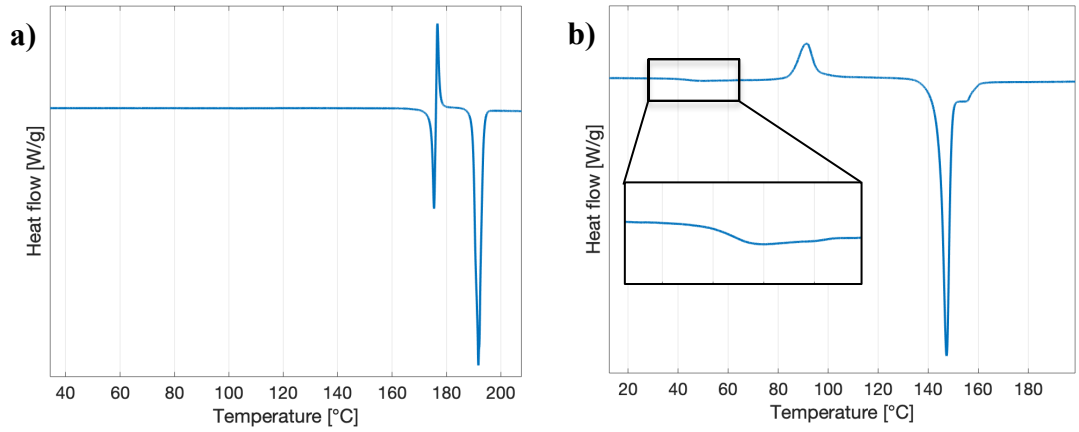

Figure 16. Thermograms of neat Carbamazepine from the a) first and b) second heating scans.

Figure 17 shows the thermograms for the amorphous solid dispersions of the hot melt extruded and solvent casted Felodipine in ethyl cellulose. The thermogram of neat ethyl cellulose prepared in the same way and neat amorphous Felodipine is added for comparison. The thermograms are taken from the second heating scan and the glass transition temperature of the compounds is described in Table 1. The thermograms of the compounds show no major difference depending on processing method.

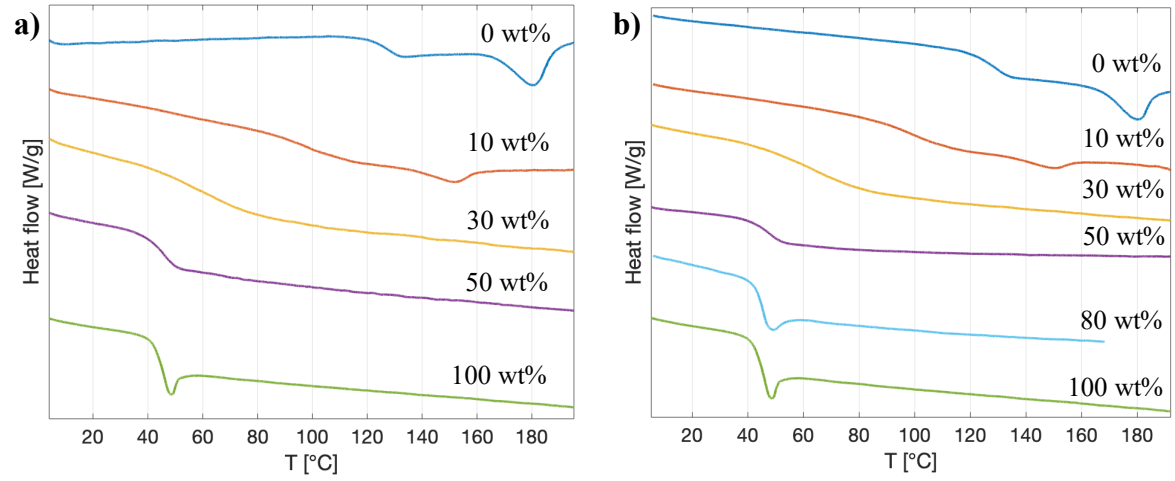

Figure 17. Thermograms from a) solvent casted and b) hot melt extruded Felodipine in Ethyl cellulose for different loadings of Felodipine (10-80 wt%) together with neat ethyl cellulose and amorphous Felodipine as a reference.

Table 1. Glass transition and melting temperatures for Felodipine, Carbamazepine and ethyl cellulose in the 1st and 2nd heating scans.

Sample	T_g 1st Scan	T_m 1st Scan	T_g 2nd Scan	T_m 2nd Scan
Felodipine	-	147°C	45°C	-
Carbamazepine	-	176°C & 193°C	45°C	145°C
Ethyl cellulose	130°C	-	130°C	-

The neat ethyl cellulose shows two transitions, a glass transition at 130 °C and melting at 180 °C, confirming that the polymer is semi crystalline. The thermogram of 10 wt% Felodipine in ethyl cellulose shows an endotherm at 150 °C which could indicate some residual crystallinity from the drug or the polymer. The melting temperature is slightly higher than what would be expected for Felodipine crystallinity and the melting endotherm disappears for the higher drug concentrations. This indicates that it most likely is polymer crystallinity that is detected. A single glass transition temperature is found for all compositions and no indications of phase separation is seen in the samples. The glass transitions of the high drug load samples, 50 and 80 wt%, are narrower and similar to that of neat Felodipine. This indicates that the molecular dynamics in the system are more similar to that of neat Felodipine. The glass transition in lower drug loads, 10 and 30 wt%, are broader. A broader glass transition can indicate heterogeneity with several phases with close glass transition temperatures that are not individually resolved.

Table 2. Glass transition temperatures and eventual melting temperatures of the amorphous solid dispersions.

Sample	T_g, Hot melt extruded	T_g, Solvent Casted
Neat EC	133 °C	130 °C
10 wt% Felo in EC	105 °C	99 °C
30 wt% Felo in EC	65 °C	64 °C
50 wt% Felo in EC	48 °C	46 °C
80 wt% Felo in EC	46 °C	-
	T_g, Hot melt extruded	**T_m, Hot melt extruded**
50 wt% Cbz in EC	56°C, 110°C	165-185°C

Figure 18 shows the thermogram of the hot melt extruded 50 wt% Carbamazepine in ethyl cellulose sample. The first heating scan (Fig. 18a) shows a broad melting endotherm ranging from 165-185 °C. Two glass transition features can also be seen at 56 °C and 110 °C. The two glass transitions indicate that there exist two amorphous phases together with the crystalline phases. The second heating scan of the hot melt extruded 50 wt% Carbamazepine in ethyl cellulose show two glass transition temperatures at 50 °C and 115 °C without any melting endotherm. This shows that the quench cooling of the heating cycle prevented the compound from crystallizing and that the drug and polymer are amorphous.

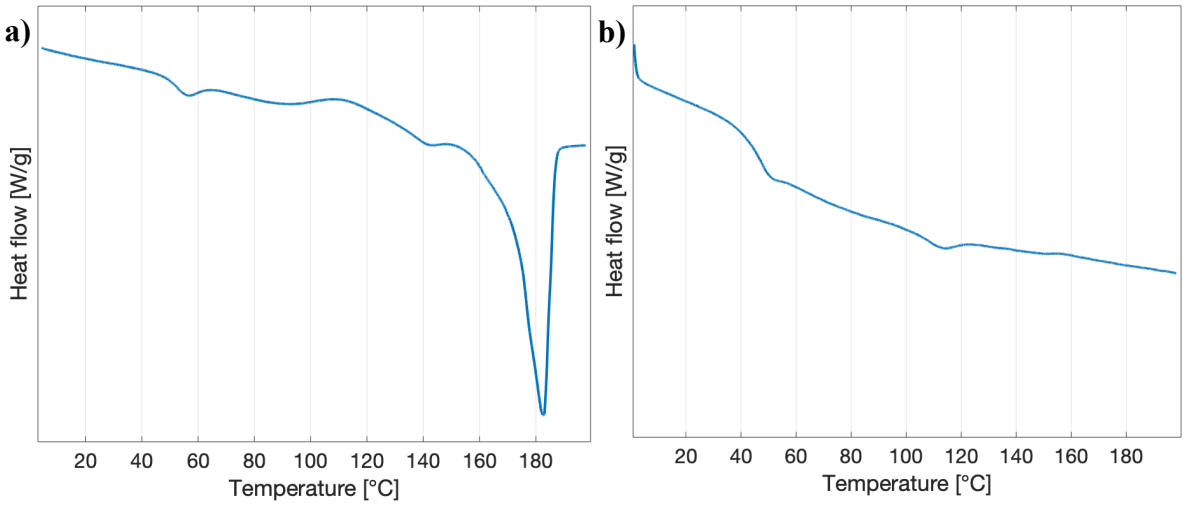

Figure 18. Thermograms of 50 wt% Carbamazepine in ethyl cellulose from the a) first and b) second heating scans.

Figure 19 shows the glass transition temperatures of the hot melt extruded Felodipine in ethyl cellulose samples as a function of drug concentration. The dotted line represents a theoretically predicted glass transitions temperatures based on the Gordon Taylor equation (*Eq. 1,* [2]) and the glass transition temperatures of the neat components. The experimental values show a negative deviation from the predicted T_g dependence on concentration which indicates that the interaction between the drug and the polymer is weaker than the homogenous interactions in the neat compound [2]. A weaker interaction between the drug and polymer favors phase separation in the system.

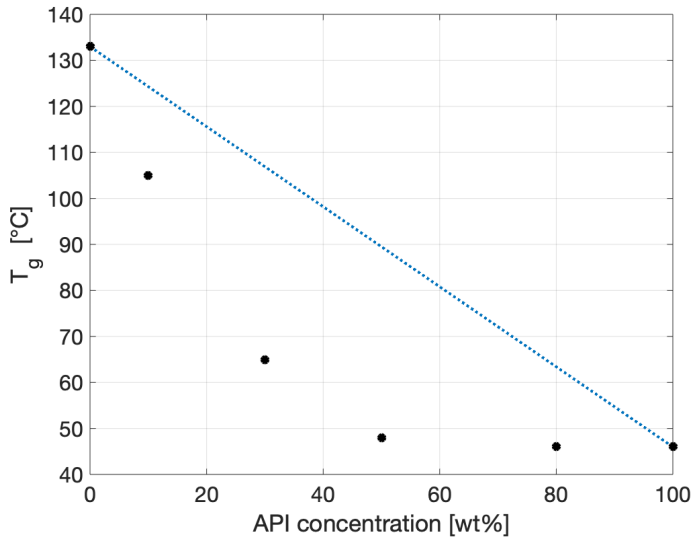

Figure 19. Measured glass transition temperatures (black) and theoretically estimated glass transition temperatures by the Gorden-Taylor equation for hot melt extruded Felodipine in ethyl cellulose.

Small-/Wide-angle-X-ray-scattering

Figure 20 shows the radial integrated SAXS and WAXS data of the solvent casted and hot melt extruded Felodipine in ethyl cellulose samples. The SAXS measurement were measured in the q-range 0.006 $Å^{-1}$ to 0.25 $Å^{-1}$ which corresponds to a length scale of 2.5-100 nm. In this q-range the curves of the hot melt extruded and solvent casted samples all show a similar slope and no distinct features are seen.

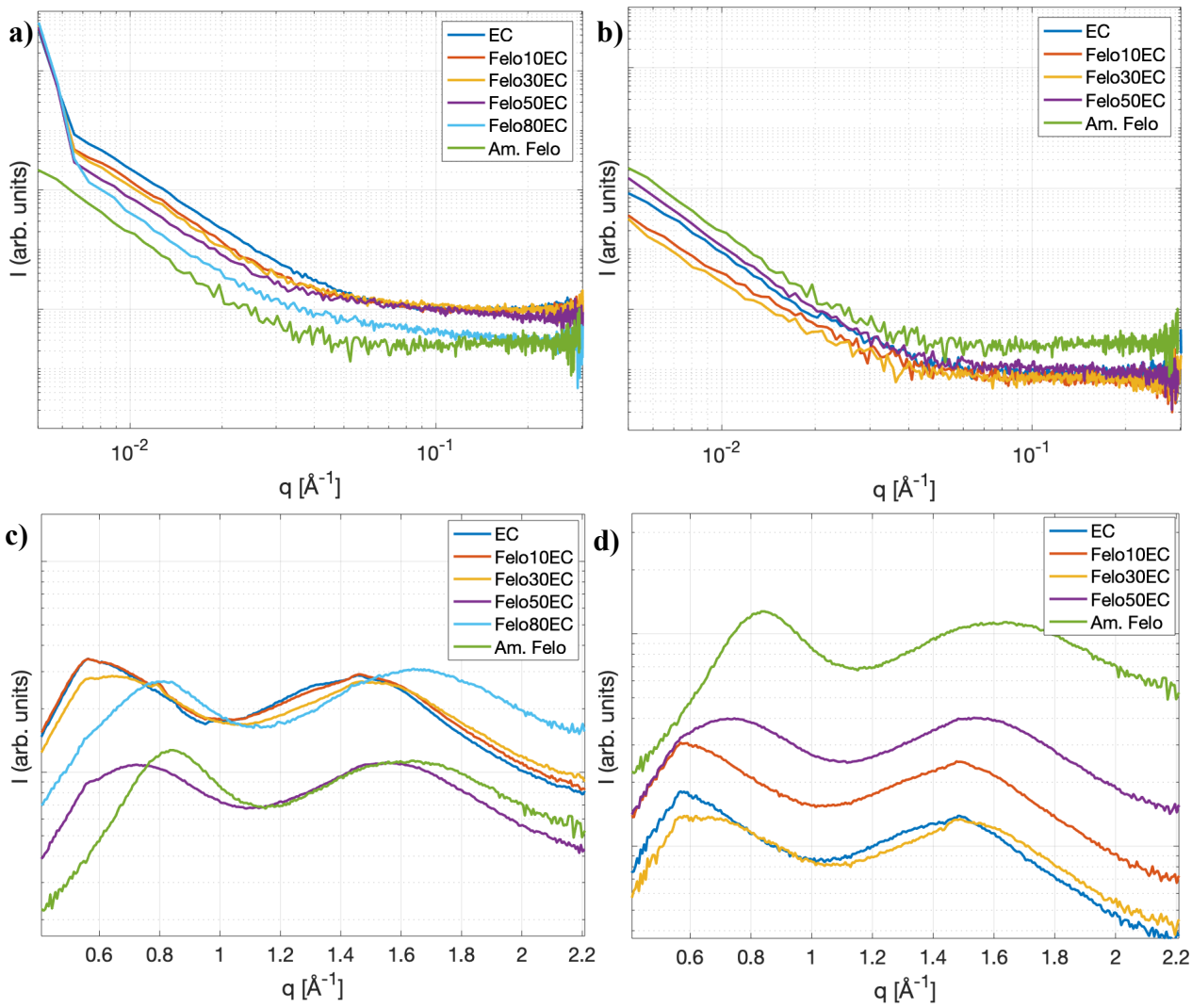

Figure 20. Scattering curves for Felodipine in Ethyl cellulose for different loadings of Felodipine (10-80 wt%) together with neat ethyl cellulose and amorphous Felodipine as a reference. The SAXS and WAXS of the hot melt extruded samples are seen in a) and c) and the SAXS and WAXS of the solvent casted samples in b) and d).

The WAXS measurement covered the q-range of 0.4 - 2.2 Å^{-1} corresponding to 0.2 - 1.5 nm, i.e. to the molecular structures. The WAXS curves of neat Felodipine and neat ethyl cellulose show two broad peaks centered at 0.84 Å^{-1} and 1.6 Å^{-1} respectively 0.57 Å^{-1} and 1.49 Å^{-1}. These amorphous halos are characteristic features in WAXS of amorphous phases. The ASDs also show two broad peaks that are shifted to higher q-values for higher drug load approaching the values for neat Felodipine. Thus, all samples show the characteristics of an amorphous system. A small peak at 0.8 Å^{-1} can be discerned for the hot melt extruded 10 and 30 wt% Felodipine in ethyl cellulose which indicates a small fraction of crystallinity of Felodipine in these samples. Similarly, in the WAXS data of the ethyl cellulose a small peak at 0.55 Å^{-1} indicate the presence of crystallinity in the polymer. The peak is present for all concentrations and indicates a small fraction of polymer crystallinity in all samples.

Figure 21 shows the SAXS and WAXS curve of the hot melt extruded 50 wt% Carbamazepine in ethyl cellulose together with the hot melt extruded neat ethyl cellulose as reference. In the SAXS curve small peaks are detecting indicating that there are features in the sample with a characteristic length scales between 10-80 nm. The large number of peaks in the WAXS pattern

of Carbamazepine indicates drug crystallinity, but the curve also shows the typical broad peaks of amorphous ethyl cellulose, indicating both amorphous and crystalline phases in the system.

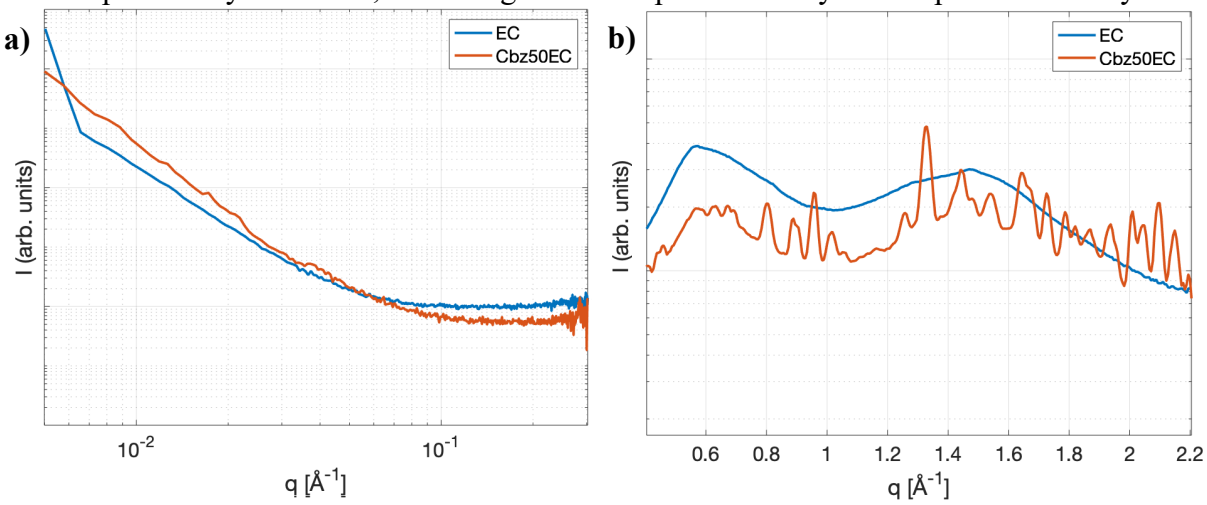

Figure 21. a) SAXS and b) WAXS curves for the hot melt extruded Carbamazepine in Ethyl cellulose together with neat ethyl cellulose as a reference.

Ptychographic X-ray computed nanotomography

The following section describes the result from the nanotomography measurements and image analysis. The results are shown both as two-dimensional electron density maps from individual slices of the tomogram as well as three-dimensional renderings of the full tomogram. Before analyzing the individual samples, a normalized cross-correlation analysis is provided for validation of the features seen in the tomograms.

Normalized cross correlation

The contrast between phases in the tomograms is dependent on the difference in the electron density between the two phases. Since the drug and the polymer are quite similar with respect to elements and have a similar electron density the tomograms have a low contrast, with respect to different phases present, and the signal to noise ratio is low. Previous studies have shown that tomograms can have correlated noise that is introduced by the filtered back projection reconstruction and the ptychographic reconstruction [25]. The correlated noise can give an impression of features present in the tomograms. To evaluate the patterns in the tomograms and distinguish the features from correlated noise, two individual measurements of the same sample were compared to evaluate the similarities of the features. Features created by noise will not be correlated between two measurements. A normalized cross correlation is computed to compare the similarities of the features in the interior sample. The correlation is also calculated for the noise, i.e. outside the sample, for comparison.

The normalized cross correlation was computed for all samples except for the 80 wt% Felodipine in ethyl cellulose due to that only one individual measurement was performed for this sample. Figure 22 shows one example of a cross correlation computed for the solvent casted 10 wt% Felodipine in ethyl cellulose. The overview of the tomogram (Fig. 22a) shows the two selected areas of the interior of the sample in blue and the noise in red. The same area is selected in both sub tomograms and the similarity between them is quantified by a correlation coefficient. The correlation coefficient is plotted on a landscape for every pixelwise off-set of the images where the center matched the correct alignment of the two sub tomograms. The maximum correlation is found to be 0.85 between the two measurements in the solvent casted sample, confirming the capability of the measurement to resolve features above the noise. No

correlation is found in the noise as seen in Figure 22c. The values of the correlation coefficient for all samples are seen in Table 3.

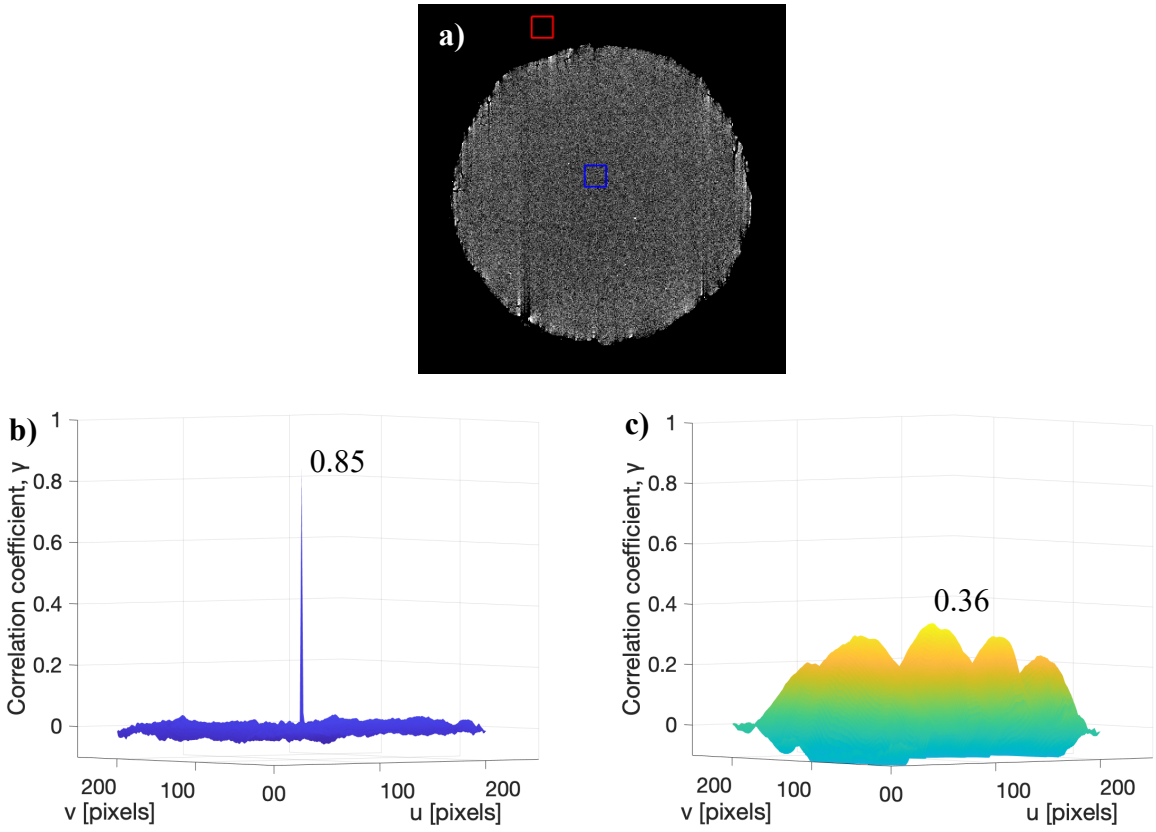

Figure 22. Normalized cross correlation of the 10 wt% solvent casted Felodipine in ethyl cellulose. a) Overview of the selected areas and the two-dimensional lanscape of the cross correlation of the b) blue area in the sample interior and c) the red area of noise outside the sample.

Table 3. Normalized cross-correlation coefficients for the tomograms.

Sample	Cross correlation coefficient
50 wt% Cbz in EC, HME	0.92
10 wt% Felo in EC, HME	0.67
50 wt% Felo in EC, HME	0.84
10 wt% Felo in EC, SC	0.85

Hot melt extruded 50 wt% Carbamazepine in ethyl cellulose

Figure 23 shows the two-dimensional electron density map of one of the center slices in the hot melt extruded 50 wt% Carbamazepine in ethyl cellulose sample. Three different phases can be distinguished with electron densities of 0.37-0.38 e/Å^3, 0.40-0.41 e/Å^3 and 0.48-0.50 e/Å^3, respectively. From these electron densities the three phases can be identified as a low-density bulk phase containing amorphous Carbamazepine and ethyl cellulose and two crystalline phases of polymorphs with different densities of Carbamazepine. The three phases are seen in Figure 23b as black, grey and white domains. The crystallinity in the sample is determined by 30 vol% from segmention of the crystalline domains from the bulk. This is also indicating that the amorphous phase consists of both Carbamazepine and ethyl cellulose. An amorphous phase of Carbamazepine in ethyl cellulose is consistent with the glass transitions that were seen in

the thermograms in Figure 18. The presence of two crystalline polymorphs are also consistent with the broader melting endotherm.

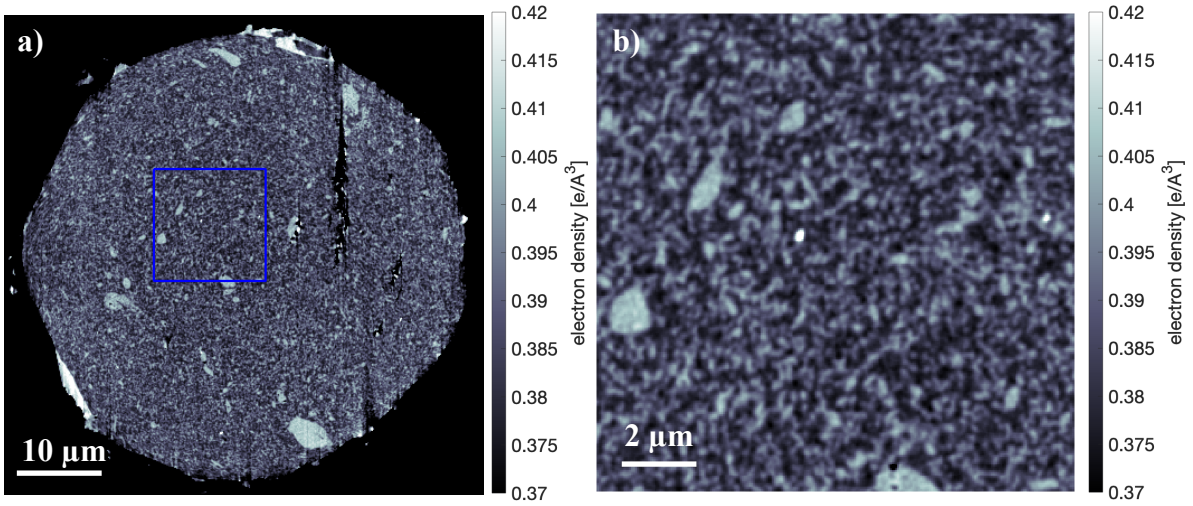

Figure 23. a) Electron density map of a center tomogram slice of the hot melt extruded 50 wt% Carbamazepine in ethyl cellulose and b) a magnified selected area marked with the blue square in a).

Figure 24 shows three-dimensional renderings of a sub volume of the sample. The polymorph with lower density, corresponding to the grey areas in Figure 23b, is segmented in orange in Figure 24a and in green in 24b and 24c. This polymorph is formed as filaments which are following the direction of extrusion and is circulating the center of the strand as is seen in the cross section of the sample in Figure 24b. The crystalline filaments have a diameter of 100-200 nm and span the entire sample. Some filaments form larger aggregates with a diameter up to a few µm. The polymorph of higher density is seen in Figure 24a as white crystallites. These crystallites are present throughout the entire volume and are also slightly elongated in the direction of the extrusion. The size of the crystallites is around 500 nm.

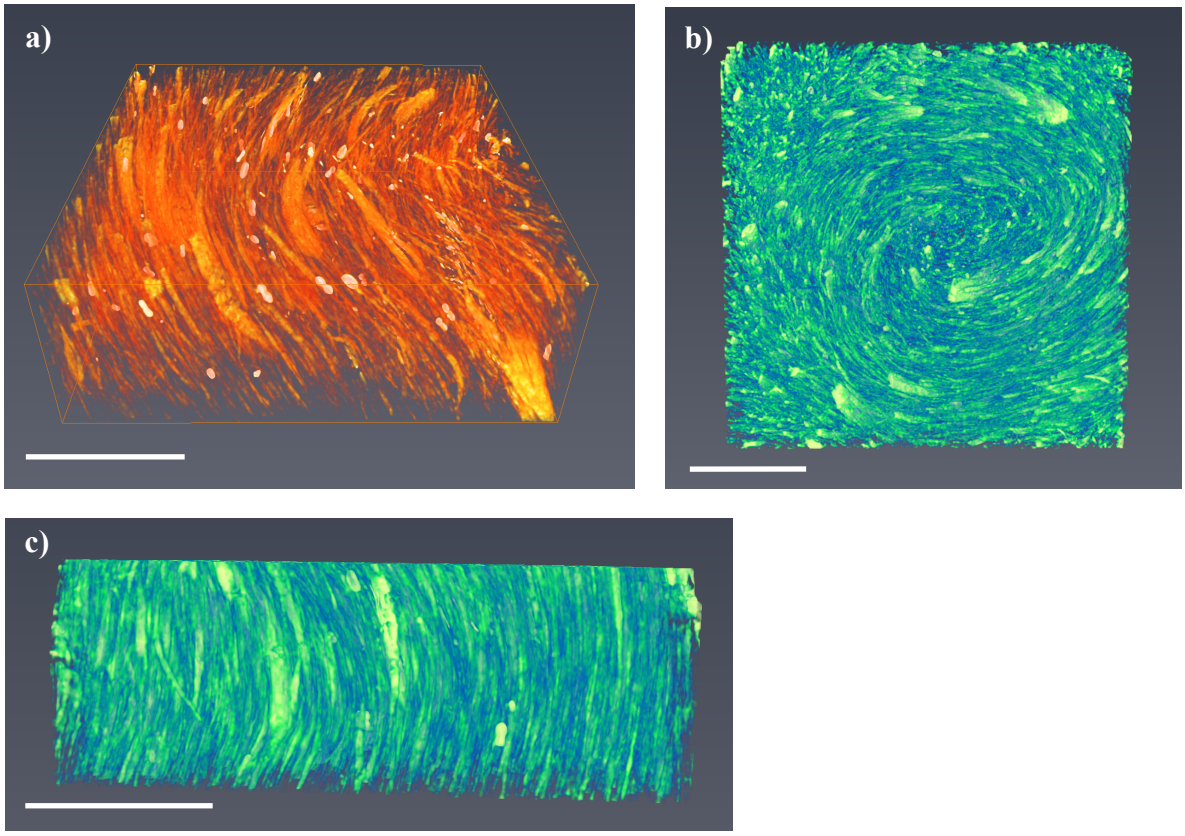

Figure 24. 3D renderings of hot melt extruded 50 wt% Carbamazepine in ethyl cellulose segmented as a) crystalline strands (orange) and crystallites (white). The orientation of the crystalline strands from a view b) parallel and c) perpendicular to the direction of extrusion. The scale bars are 10 µm.

Hot melt extruded 50 wt% Felodipine in ethyl cellulose

Figure 25 shows the two-dimensional electron density map of one of the center slices in the hot melt extruded 50 wt% Felodipine in ethyl cellulose sample. The tomogram slice shows a connected pattern of domains with a gradual change from high to low electron density. This pattern is similar to characteristic patterns of a spinodal decomposition [17] and has a characteristic domain size of 200-300 nm. The electron densities of the two phases are between 0.39-0.395 e/Å^3 and 0.395-0.4 e/Å^3, respectively, which corresponds to two mixed amorphous phases. The concentration of the mixed phases can be estimated from the electron density with the assumption that the electron densities of the drug and polymer are additive and that the probed sample is not deviating from the nominal bulk concentration, 50 wt% drug loads. Using that estimation, the compositions of the two phases are of 50-60 wt% and 40-50 wt% drug respectively. Figure 26 shows the three-dimensional morphology of a sub volume of the sample. The renderings clearly show the high connectivity of the domains over the sample.

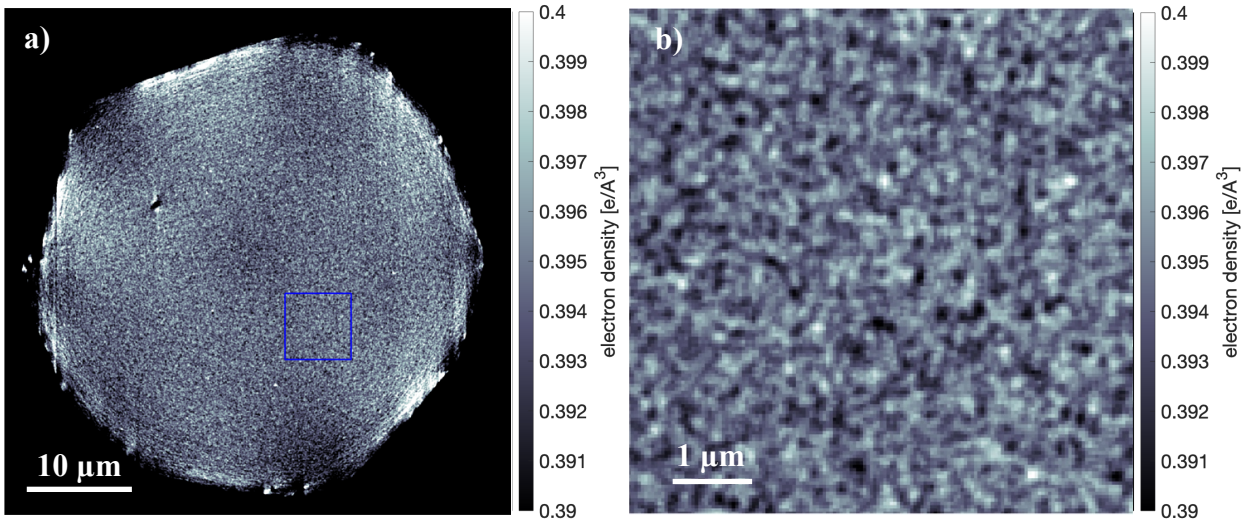

Figure 25. Electron density map of a center tomogram slice of the hot melt extruded 50 wt% Felodipine in ethyl cellulose and b) a magnified selected area marked with the blue square in a).

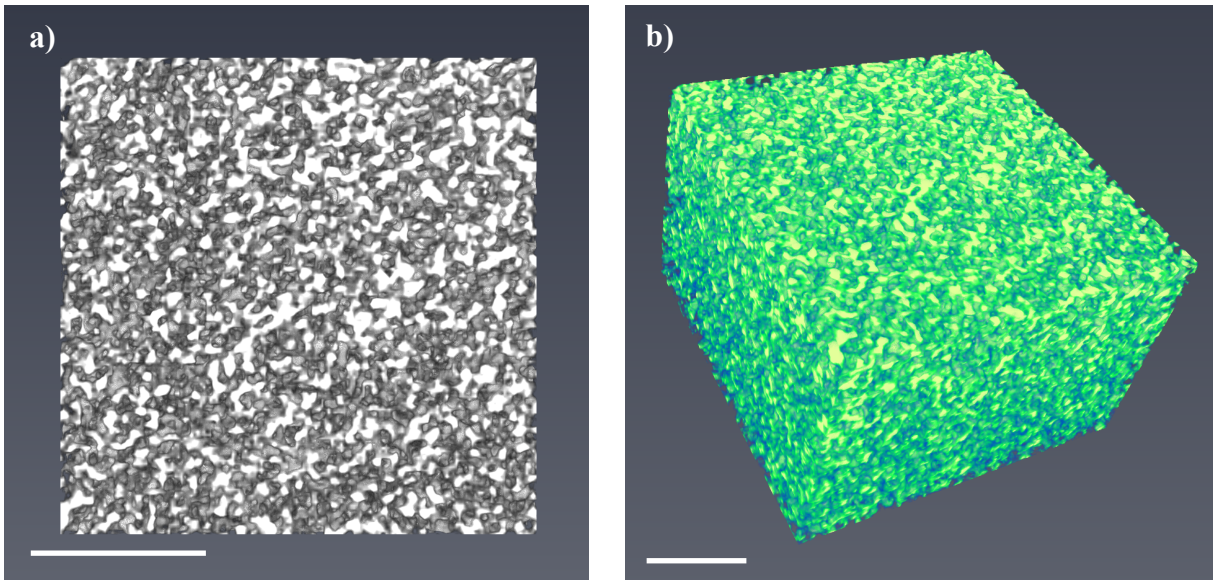

Figure 26. 3D renderings of hot melt extruded 50 wt% Felodipine in ethyl cellulose. The scale bars are 2 µm.

In addition to the two amorphous phases a small amount of crystallinity is found to be present in the sample. Figure 27a shows a two-dimensional slice of an area of the sample that contains a crystallite together with a three-dimensional segmentation of the crystallites in a sub volume of the sample. The green and blue areas in Figure 27a show the amorphous drug rich and drug poor domains and the red spot is a crystallite which has an electron density of 0.44-0.45 e/Å^3. The electron density matches the theoretical value for crystalline Felodipine, thus the segmented particles in Figure 27b corresponds to crystallized drug. Most of the crystallites are approximately 100-200 nm but there are also a few bigger particles, approximately 400-500 nm. The crystallites are randomly distributed over the measured sample volume with a volume fraction of <0.1%.

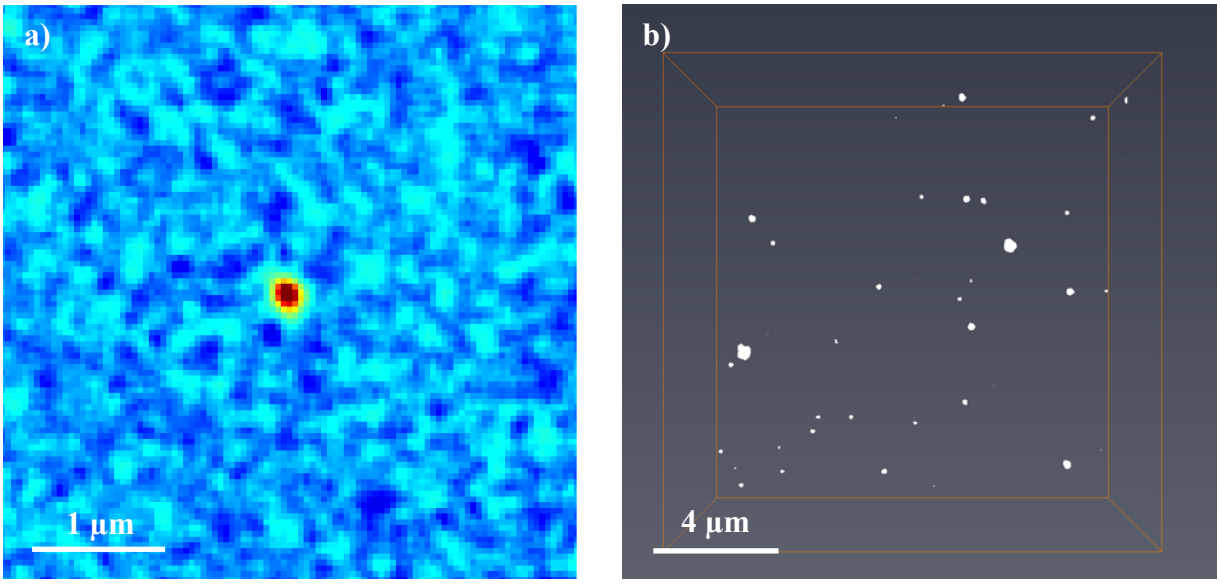

Figure 27. a) 2D segmentation of a crystallite (red) and drug rich (green) and drug poor (blue) domains in hot melt extruded 50 wt% Felodipine in ethyl cellulose and b) 3D segmentation of the crystallinity in a subvolume of the sample.

Hot melt extruded 10 wt% Felodipine in ethyl cellulose

Figure 28 shows the two-dimensional electron density map of one of the center slices in the hot melt extruded 10 wt% Felodipine in ethyl cellulose. Figure 28a reveals a big crack in the sample. The edge of the crack creates artefacts, e.g. straight lines in the tomogram parallel to the crack. The normalized cross correlation between the two sub tomograms is 0.67 which is slightly lower correlation than for the 50 wt% sample (Tab. 2). The lower correlation coefficient could indicate that there is more noise in the tomograms for this sample which partly conceals the nanostructure.

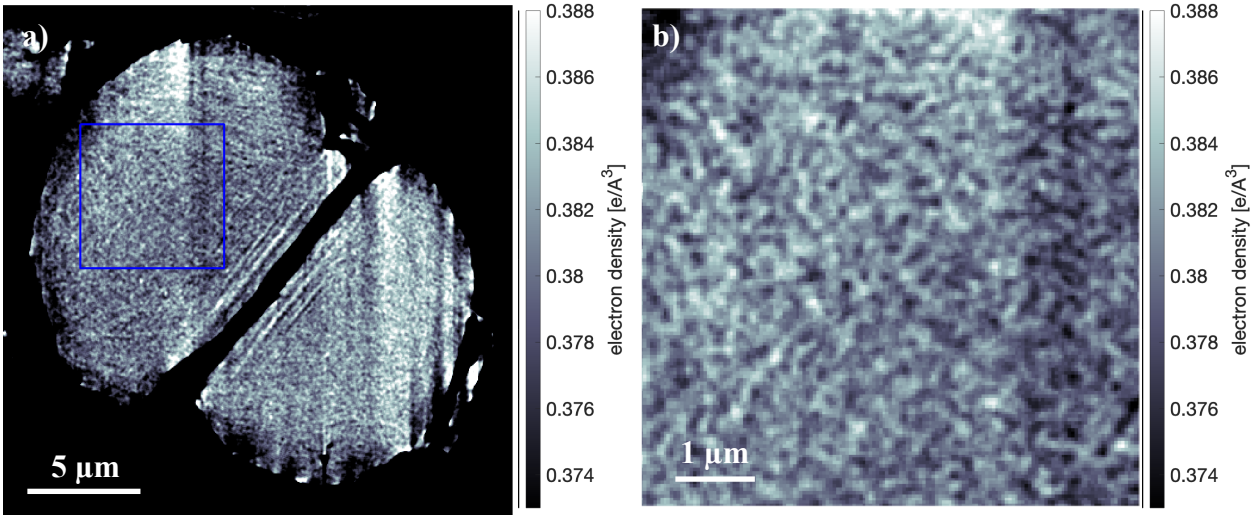

Figure 28. Electron density map of a center tomogram slice of the hot melt extruded 10 wt% Felodipine in ethyl cellulose and b) a magnified selected area marked with the blue square in a).

The electron density map in Figure 28b shows a connected, random pattern of domains with a gradual change from high to low electron density, similar to the pattern found for 50 wt% Felodipine in ethyl cellulose sample. The three-dimensional rendering of the sample is seen in Figure 29. The characteristic length scale of the domains is 200-300 nm and the electron densities of the phases are 0.373-0.381 e/Å^3 to 0.381-0.388 e/Å^3. The composition of the phase, assuming additivity of the electron density, is estimated to 0-15% and 15-30%. The average value of the electron density in the full tomogram is higher than expected of a sample with a concentration of 10 wt%. These errors in the estimation of the composition can depend on several factors. The concentration of the smaller probed sample can fluctuate from the nominal 10 wt%, the additivity of the electron density is an assumption and noise and artefacts in the sample may disturb the average value of the electron density.

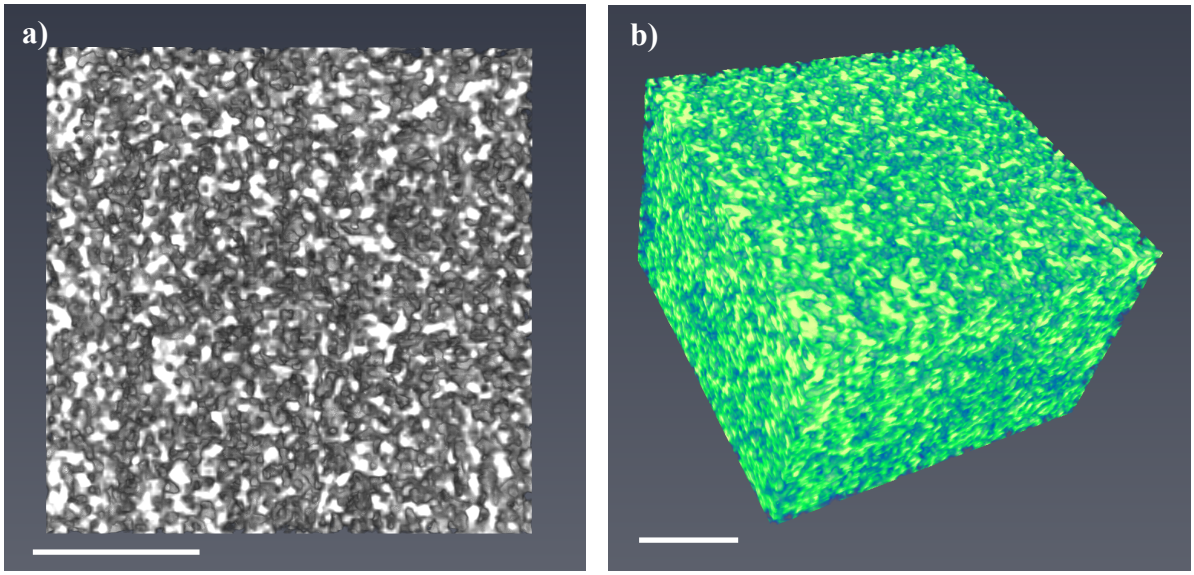

Figure 29. 3D renderings of hot melt extruded 10 wt% Felodipine in ethyl cellulose. The scale bars are 2 µm.

Figure 30 shows a two-dimensional slice of an area of the sample that contains a crystallite together with a three-dimensional segmentation of the crystallites (0.44-0.45 e/Å^3) in a sub volume of the sample. A larger aggregate of crystallites can be distinguished in the lower left of Figure 30b. This aggregate is located around a pore in the sample. The size of the crystallites in the intact bulk area of the sample is 100-200 nm. Larger regions of high electron densities (0.44-0.45 e/Å^3) are also found at the interface of the crack (circled in Figure 30b). These regions can be artefacts from the sharp edge in the sample or indicate an increased crystallinity around the cracked surface. The crystallinity is <0.1 vol% and is expected to be even lower without the crack, i.e. in an intact bulk sample.

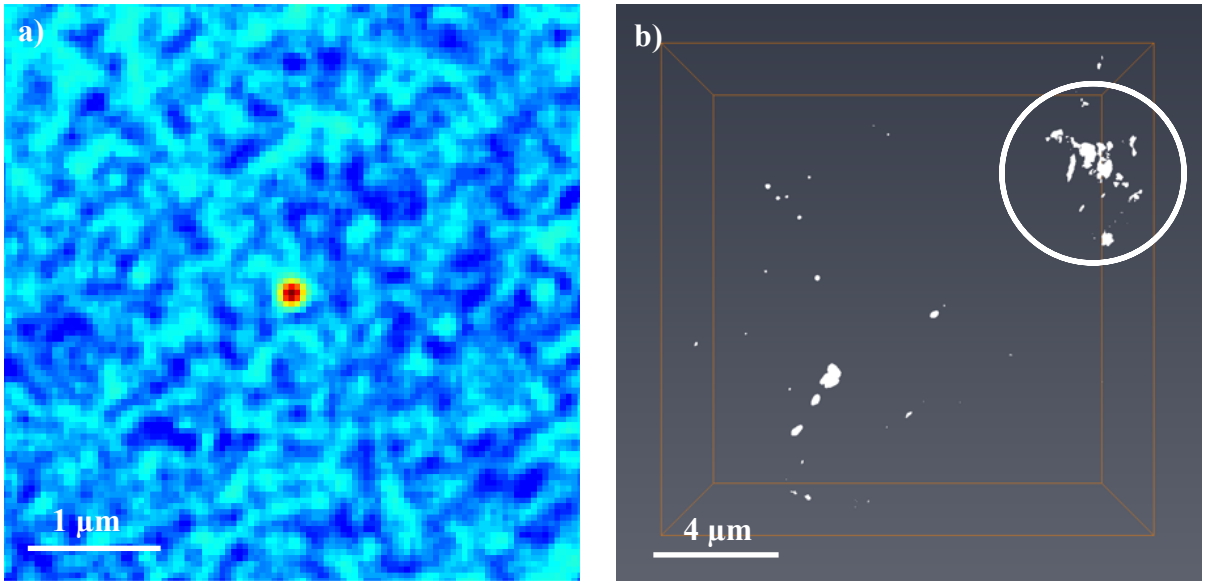

Figure 30. a) 2D segmentation of a crystallite (red) and drug rich (green) and drug poor (blue) domains in hot melt extruded 10 wt% Felodipine in ethyl cellulose and b) 3D segmentation of the crystallinity in a subvolume of the sample.

Hot melt extruded 80 wt% Felodipine in ethyl cellulose

For the hot melt extruded 80 wt% Felodipine in ethyl cellulose sample a single sub tomogram was recorded due to time limitations which prohibits computing a cross correlation between individual measurements. Figure 31a shows an overview of the sample and reveals an irregular shape with several edges which creates artefacts, as seen as straight lines from corners in the sample. As for the hot melt extruded 10 wt% Felodipine in ethyl cellulose sample, this has to be taken into consideration during evaluation of the data.

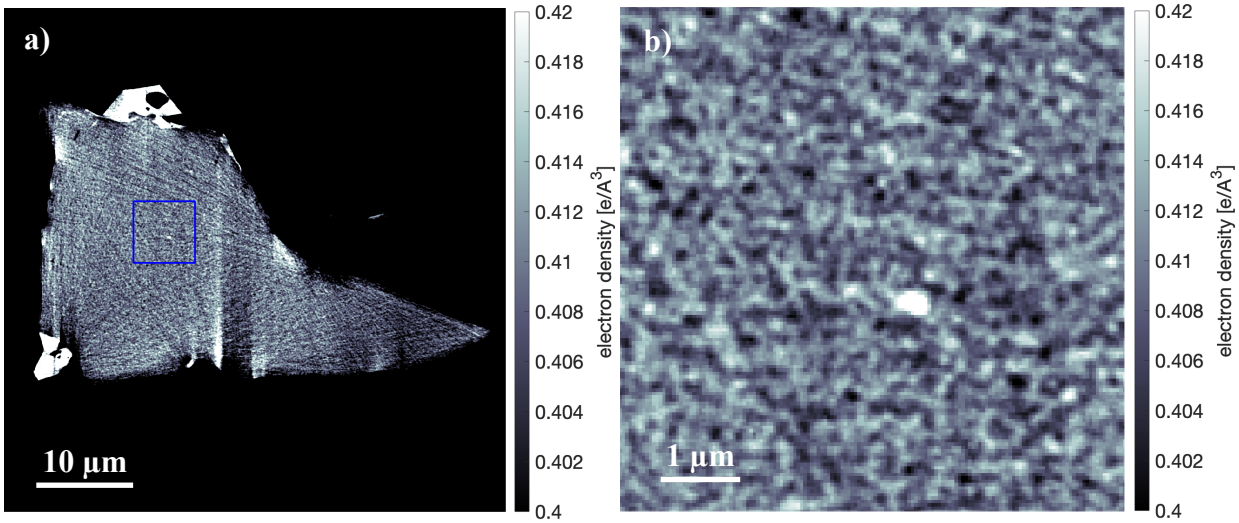

Figure 31. Electron density map of a center tomogram slice of the hot melt extruded 80 wt% Felodipine in ethyl cellulose and b) a magnified selected area marked with the blue square in a).

The electron density map in Figure 31b shows a connected, random pattern with gradually changing high and low electron density phases as for the other hot melt extruded samples. The electron densities of the phases are 0.4-0.41 e/Å^3 and 0.41-0.42 e/Å^3 and the characteristic length scale is 200-300 nm. The composition of the phase, assuming additivity of the electron density, is estimated to 60-80 wt% and 80-100 wt% drug. This sample has a larger fluctuation in electron densities and compositions of the phases compared to the lower drug concentration samples. Figure 32 shows the three-dimensional rendering of the sample.

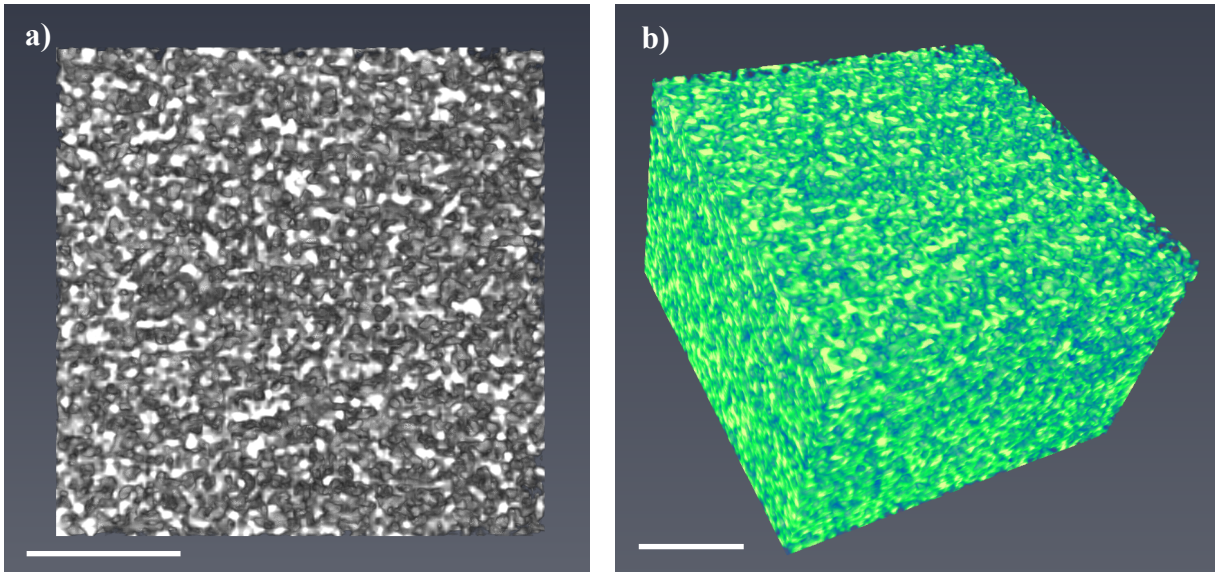

Figure 32. 3D renderings of hot melt extruded 80 wt% Felodipine in ethyl cellulose. The scale bars are 2 µm.

Despite indications of a increased phase separation, the crystallinity in this sample is still low, <0.1 vol%. Figure 33 shows the segmentation of crystallites with electron density of 0.44-0.45 e/Å^3.

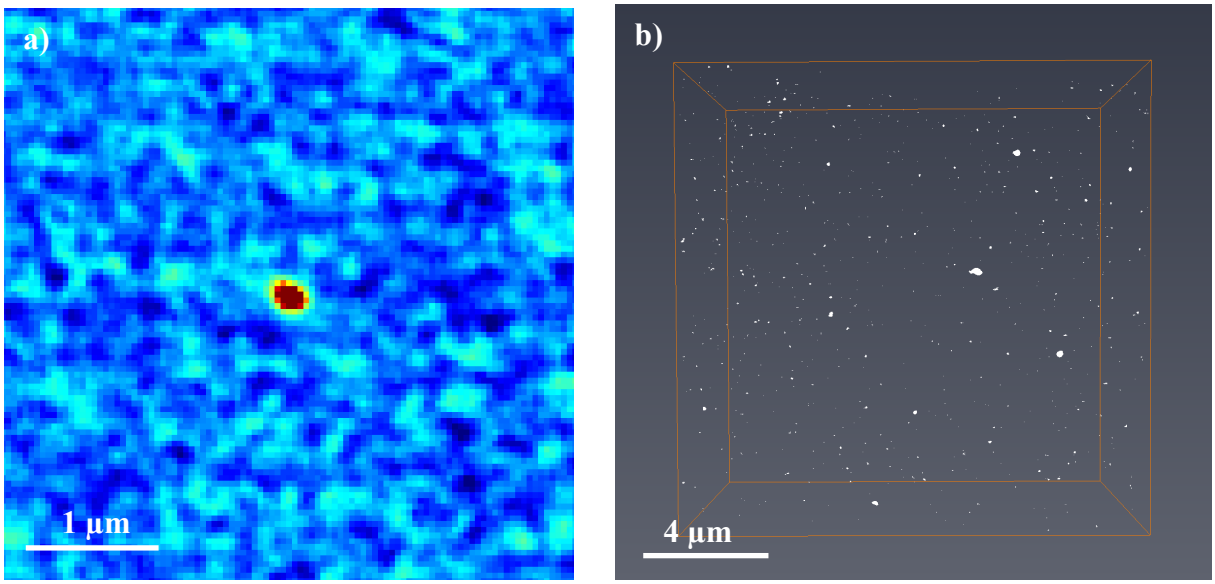

Figure 33. a) 2D segmentation of a crystallite (red) and drug rich (green) and drug poor (blue) domains in hot melt extruded 80 wt% Felodipine in ethyl cellulose and b) 3D segmentation of the crystallinity in a subvolume of the sample.

Solvent casted 10 wt% Felodipine in ethyl cellulose

Figure 34 shows the two-dimensional electron density map of one of the center slices in the solvent casted 10 wt% Felodipine in ethyl cellulose sample. The solvent casted sample has large spherical domains of low electron density separated by narrow domains of high electron density. The respective sizes are 2 µm and 300 nm and the electron densities around 0.37 e/Å^3 and 0.375 e/Å^3 in the two phases. Assuming additivity of electron density and no fluctuation from the nominal 10 wt% drug load, this correspond to a phase separation into a low-density phase close to pure polymer and one phase close to 20 wt% drug loads. Figure 35 shows the three-dimensional rendering of the sample.

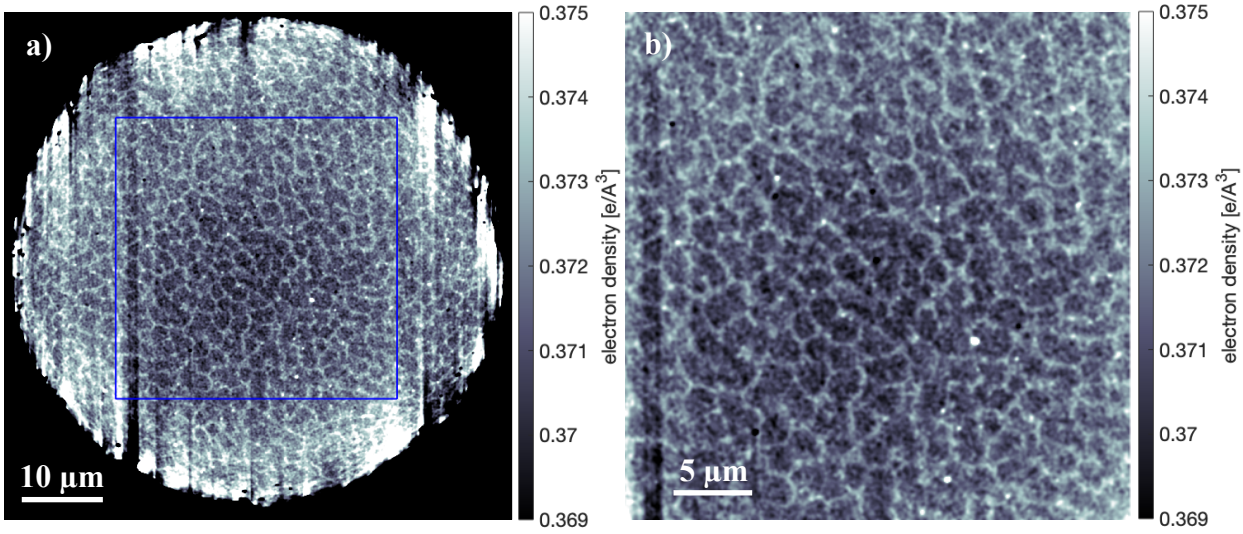

Figure 34. Electron density map of a center tomogram slice of the solvent casted 10 wt% Felodipine in ethyl cellulose and b) a magnified selected area marked with the blue square in a).

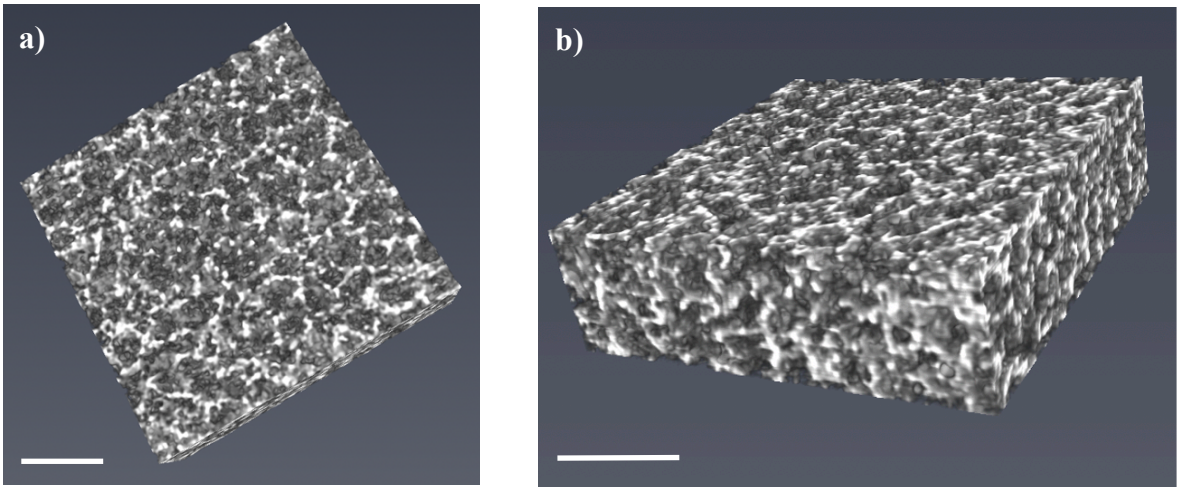

Figure 35. 3D renderings of solvent casted 10 wt% Felodipine in ethyl cellulose. The scale bar is 2 µm.

Figure 36 shows the segmentation of crystallites with electron density of 0.44-0.45 e/Å^3. The crystallites all appear in the high density, drug rich phase as seen in Figure 36a. The size of the crystallites is 200-400 nm and a volume fraction of crystalline phase is <0.1%.

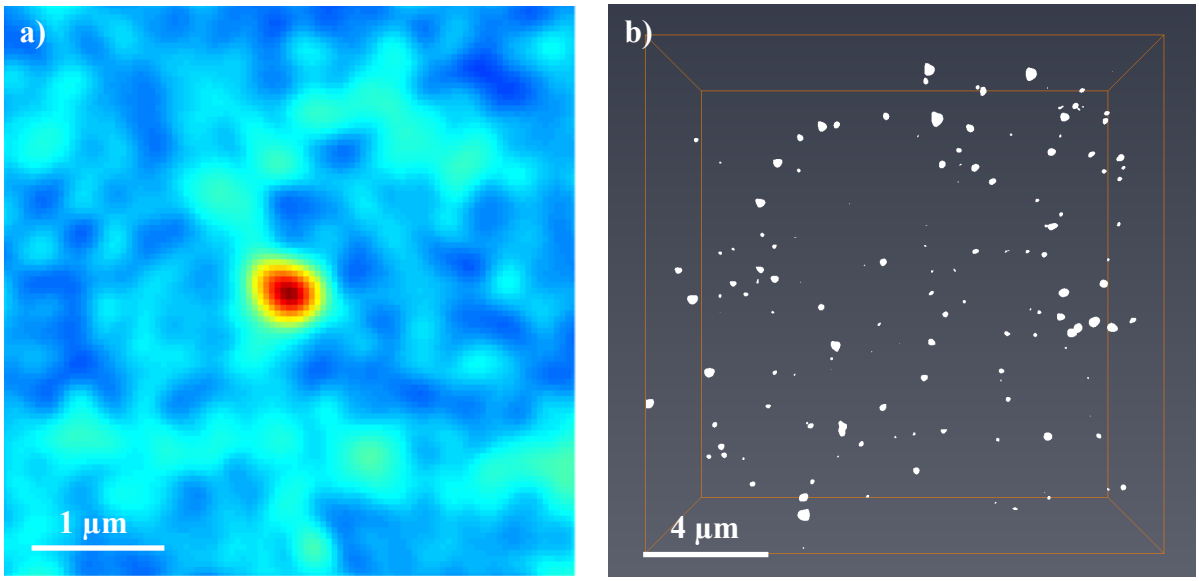

Figure 36. a) 2D segmentation of a crystallite (red) and drug rich (green) and drug poor (blue) domains in the solvent castes 10 wt% Felodipine in ethyl cellulose and b) 3D segmentation of the crystallinity in a subvolume of the sample.

Comparison of results from different characterization methods

One important difference between the results from the DSC and S/WAXS measurements and the nanotomography is that the first two measurements are made on millimeter sized samples while the nanotomography measures micrometer sized samples. The tomography sample is extracted from the center of the bulk sample and possible edge effects should not influence the result. In addition, the tomography will not detect if there are variations in the sample on larger length scales than 10-20 µm. The morphology found in the tomogram is therefore representative of the center of the sample. Since the DSC and S/WAXS probes a larger volume of the sample, the methods might show differences in the results if it detects spatial variations that remains undetected by the tomography.

Another important aspect to have in mind is that the DSC is a non-isothermal technique. During heating the mobility of the drug and polymer increases which might lead to a remixing of the system during the measurement and may result in an undetected phase separation. Previous studies have shown that an amorphous solid dispersion with a phase separation on micron scale still shows a single glass transition in DSC, misleadingly indicating a homogenous system [23].

The DSC measurement of the 50 wt% Carbamazepine in ethyl cellulose sample showed both glass transitions as well as melting, indicating a system containing both amorphous and crystalline phases. The glass transition temperatures points to an amorphous phase containing both ethyl cellulose and Carbamazepine. The presence of both a crystalline drug phase and an amorphous phase containing ethyl cellulose was also shown by the WAXS measurements. The nanotomography is in agreement with this result and provided additional information of the distribution of the two crystalline polymorphs in the amorphous bulk matrix. The tomography results are also in agreement with the DSC results in that the amorphous phase is composed of both ethyl cellulose and Carbamazepine and the presence of crystalline Carbamazepine. The SAXS curve showed that there are features in the sample with a characteristic length scales between 10-80 nm. These cannot be seen in the nanotomography results due to a size smaller than the resolution.

Neither the SAXS in the measured q-range nor the DSC measurement provide evidence of phase separation in any of the Felodipine in ethyl cellulose samples. In contrast, the tomography measurement showed a phase separation on a length scale of a few 100 nm. This explains why they are not detected in the SAXS measurements as they are larger than the length scales probed in this experiment. DSC has shown limitations in detecting phase separation [23], as described above, and as the phases are fairly close in composition it is likely that the T_gs will also be quite close and the phase separation remain undetected.

The DSC measurements of the Felodipine in ethyl cellulose samples showed no evidence of crystallinity. A small amount of drug crystallinity was detected in the hot melt extruded 10 and 30 wt% samples by the WAXS measurements as well as polymer crystallinity in all compositions. Polymer crystallinity was also seen in the thermograms of both the HME and SC 10 wt% Felodipine in ethyl cellulose samples. The nanotomography revealed crystallinity as low as <0.1vol% in all Felodipine in ethyl cellulose samples. The electron density of the crystallites was determined to 0.44-0.45 e/Å^3 which corresponds to crystalline Felodipine. No theoretical value of the density of crystalline ethyl cellulose has been reported but if the density of crystalline ethyl cellulose would be 5-15% higher than that of the amorphous form it would correspond to an electron density of 0.39-0.425 e/Å^3. Since this is still lower than the electron density of the crystallites in the tomograms those are assigned as drug crystallites. Polymer crystallites were not identified by tomography due to the uncertainty of their electron densities and that most likely their density is close to that of the bulk phase in many of the samples.

The effect of processing method on the morphology of the dispersion

The high crystallinity and elongated morphology of the hot melt extruded 50 wt% Carbamazepine in ethyl cellulose sample is most likely a result of the drug not being fully melted during the extrusion process ($T_{process}$∼180 °C, T_m∼170-190 °C). The extrusion process involves a high sheer which created the directional pattern of the crystalline strands seen in the tomograms. A high degree of crystallinity was expected due to the low temperature with respect to the melting point of Carbamazepine used during the extrusion.

The Felodipine in ethyl cellulose samples prepared by hot melt extrusion all show a pattern with connected domains, characteristic for phase separation through spinodal decomposition. The 10 wt% Felodipine in ethyl cellulose sample prepared by solvent casting instead shows large spherical domains separated by narrow domains, indicating a phase separation through nucleation and growth. These results suggest that the two processing methods result in different morphologies induced by different phase separation mechanism.

The phase separation mechanism can be discussed in context of the immiscibility regions for the compound during the hot melt extrusion process. Figure 37 shows a schematic phase diagram for the binary mixture of drug and polymer. Theoretical models have shown that the phase diagrams of ASDs have a broad unstable region, as illustrated in Figure 37 [51]. In hot melt extrusion the drug and polymer are mechanically mixed in their molten states, i.e. ideally the process temperature is above the melting point of both components. After being extruded, the mixture cools to room temperature and will pass the coexistence curve separating the stable and unstable regions. When the spinodal line is crossed the sample will start to phase separate immediately through spinodal decomposition. The mobility of the system is high at high temperatures but decreases as the temperature approaches the glass transition temperature. When the glass transition temperature is crossed the sample will freeze into a solid and further phase separation is hindered. The compositions of the phases calculated from the tomograms show that the three hot melt extruded Felodipine in ethyl cellulose samples have not reached

the coexisting compositions suggesting that the spinodal decomposition is stopped in an early stage by passing the glass transition temperature. The gradient of the composition is still small and the edges between domains are diffuse which is also indicating that the phase separation is in an early stage. [51]

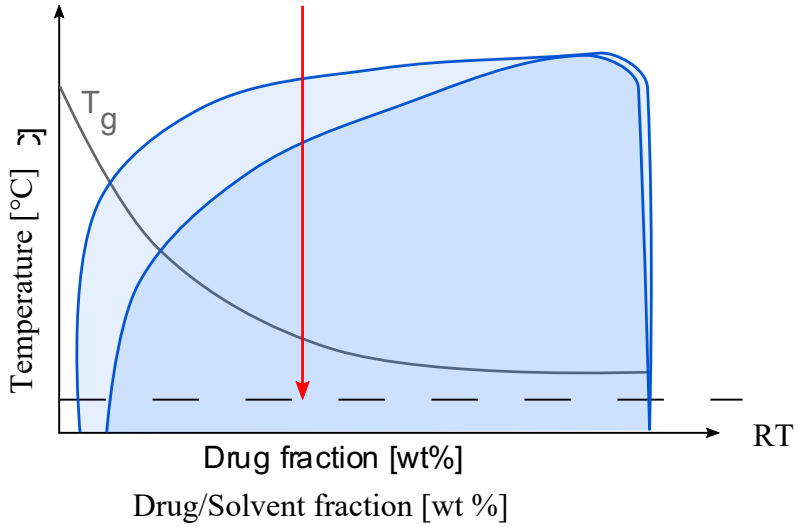

Figure 37. Schematic phase diagram for Felodipine in Ethyl cellulose. The outer blue curve represents the coexistence curve and the inner blue curve the spinodal line and the unstable and metastable regions are highlighted in blue. The glass transition temperature is illustrated in grey and the dotted line marks ambient temperature. The red arrow shows the path for a hot melt extruded ASD of a certain composition during cooling.

In solvent casting we have to consider a ternary system due to the addition of the solvent. Figure 38 shows a schematic ternary phase diagram for the drug and polymer dissolved in a solvent where the red arrow symbolizes the evaporation of solvent. During the solvent casting process the drug and the polymer are mixed with a solvent until they are fully miscible, i.e. outside the coexistence curve. The solvent will reduce the glass transition temperature of the compound and the mobility in the system will be high. After being casted, the solution starts to evaporate and at some point, the system will reach the miscibility limit and start to demix. From the morphology in the solvent casted Felodipine sample, (Fig. 34), it is suggested that phase separation occurs in the metastable region through nucleation and growth. If nucleation is initiated, the phase separation will continue to grow during evaporation until the glass transition temperature of the compound reaches ambient temperature. Figure 38 schematically illustrates a hypothetical phase diagram that would create the phase separation pattern seen in the solvent casted sample.

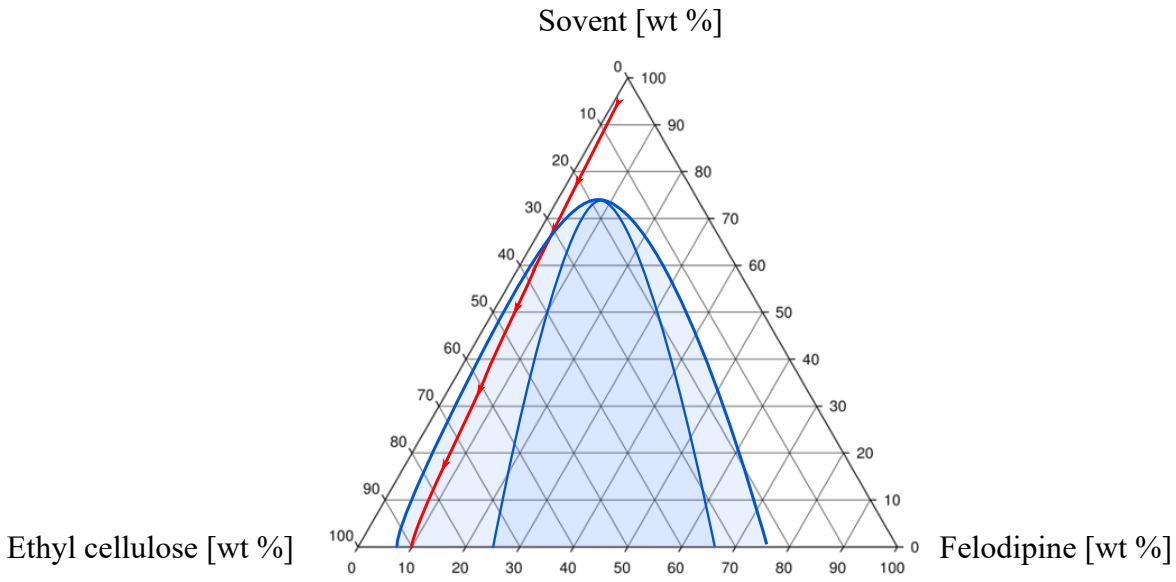

Figure 38. Schematic ternary phase diagram of the drug and polymer dissolved in a solvent. The unstable and metastable regions are highlighted in blue. The red arrow marks the path for the system during evaporation.

From the electron density in the tomograms the nucleated domains are determined as polymer-rich domains, with a composition close to neat ethyl cellulose. During nucleation and growth, the minority phase is the one that nucleates [52], suggesting that the polymer was the minority phase when the nucleation process started. The polymer can be seen as the minority phase early in the evaporation process when the solvent concentration is high as the solvent and the drug are both small molecules and are distinctively different from the polymer. This suggest that the drug is more miscible with the solvent than the polymer and that the phase separation starts at a rather high concentration of solvent, as schematically illustrated in Figure 38. A higher miscibility between the drug and the solvent than the polymer and the solvent were also observed during the preparation of the solvent casted films.

The spherical domains in the solvent casted sample have a size of a few micrometers which indicates a significant growth of the nucleus during the phase separation process. To allow for a significant growth, the system needs to be in the metastable state during an extended time period and have a sufficiently high mobility. This means that the evaporation should be sufficiently slow and that the miscibility limit should be reached when the glass transition temperature of the system is well below the ambient temperature, which also points to the fact that the phase separation should start at a rather high concentration of solvent. Previous studies on similar amorphous solid dispersions using fluorescence imaging [6] have also shown that nucleation and growth occurred during solvent evaporation and that the size of the nucleus is dependent on the evaporation rate. It was also shown that solvent casted samples had a size of a few micrometers which is consistent with the results in this thesis.

Figure 39 shows an additional type of schematic phase diagram of the ternary system of the miscibility regions as a function of temperature and drug/solvent fraction. Here, the drug and solvent concentrations are combined, and the red arrow symbolizes the path through the phase diagram during evaporation. When the coexistence curve is reached, the system enters the metastable region where nucleation can occur. During continued evaporation the glass transition temperature of the solution will increase and eventually reach ambient temperature and the solution will freeze into a solid film and the phase separation will be hindered.

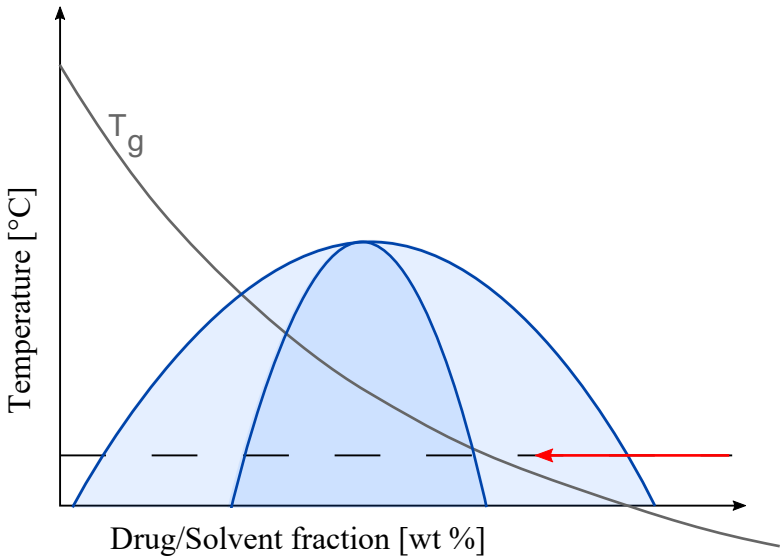

Figure 39. Schematic phase diagram for Felodipine in Ethyl cellulose. The outer blue curve represents the coexistence curve and the inner blue curve the spinodal line and the unstable and metastable regions are highlighted in blue. The glass transition temperature is illustrated in grey and the dotted line marks ambient temperature. The red arrow shows the path for a solvent casted ASD during evaporation.

Another interesting feature observed in the morphology of the Felodipine in ethyl cellulose samples, which are specifically clear for the solvent casted sample, are that the drug crystallites all appear in drug rich domains. This points to the fact that phase separation has a great impact on the possibility of keeping the drug stable in its amorphous form as has been stressed before [4]. The drug rich phase contains less polymer in the mixture which could mitigate the stability in that domain and a higher concentration of drug will increase the possibility of aggregates of drug molecules which can crystallize.

The effect of drug concentration on the morphology of the dispersion

The three hot melt extruded samples of Felodipine in ethyl cellulose all show a phase separation pattern characteristic of spinodal decomposition. The domain size is similar for all concentrations, but the concentration differences between the two phases are higher for the 80 and 10 wt% Felodipine in ethyl cellulose samples. From calculations of the composition of the phases the 80 wt% sample differs with about 40 wt% between the two phases. The corresponding numbers are about 30 wt% and 20 wt% for the 10 and 50 wt% samples respectively. The phase diagram related to the hot melt extrusion process in Figure 37 suggests that the system will be in the unstable region for a longer period during cooling at higher drug concentrations. This will extend the time spent in the unstable region where phase separation occurs before reaching the glass transition which would explain the more pronounced phase separation seen in the 80 wt% Felodipine sample. Another contributing factor could be that the dynamics in the system is faster at higher drug concentration [51], thus there is a larger mobility in the system which can result in a more pronounced phase separation.

The more pronounced phase separation in the 10 wt% sample is more difficult to explain. At lower drug concentration the mobility in the system is expected to be lower and the glass transition temperature is higher, reducing the time for phase separation. As discussed in connection to the tomography results for the 10 wt% sample, the crack in the sample together with a lower correlation coefficient could suggest that the measurement quality was poorer. A poorer measurement quality could give a wider noise distribution, falsely indicating a wider

range of contrast between the two phases. This could also be a factor for the 80 wt% Felodipine in ethyl cellulose sample as it was only measured with one sub tomogram.

For the solvent casted samples only one concentration was measured, 10 wt% Felodipine in ethyl cellulose. Therefor it is not possible to say anything about how the concentration would affect the morphology of the solvent casted samples. It is possible that it would affect the extent of phase separation, but it is also possible that it would have another mechanism of phase separation and may produce another type of morphology from the solvent casted 10 wt% Felodipine in ethyl cellulose.

Conclusion and Outlook

Conclusion

In conclusion, phase separation was detected in all amorphous solid dispersions. The ptychographic X-ray nanotomography was able to resolve the morphology of the ASDs and provide additional information on phase separation and crystallinity that was not detected with DSC or X-ray scattering. The nanotomography showed capability of probing electron density fluctuations of below 0.1 e/Å and resolve two very similar phases at a resolution of 100 nm. A higher resolution is expected to be possible to reach by optimizing the sample preparation and creating smaller pillars together with optimized measuring parameters found during this study. The successful results of the ptychographic nanotomography in being able to resolve the morphology of amorphous solid dispersions also pave way for performing the same analysis on similar systems, e.g. polymeric materials or other pharmaceutical compounds.

The morphology found in the solvent casted respectively hot melt extruded Felodipine in ethyl cellulose samples indicates that the different processing methods generates a phase separation through different mechanisms. The hot melt extruded samples phase separated through spinodal decomposition while the solvent casted sample phase separated through nucleation and growth. This can be connected to their different ways of forming the amorphous solid and reaching the glass transition temperatures. The result of the effect on the morphology shows that the processing parameters can be crucial to be able to mitigate phase separation and rationally design a dispersion.

The morphology found in the 50 wt% hot melt extruded Carbamazepine in ethyl cellulose showed a result of an extrusion at a temperature too low to enable successful melting. This induced a high crystallinity in the sample and shows the high sheer induced by the extrusion method that produced a high directionality of the phases in the extruded strand. The unsuccessful melting and mixing of Carbamazepine and ethyl cellulose showed that hot melt extrusion is not suitable for this specific ASD.

The morphology of the hot melt extruded Felodipine in ethyl cellulose showed a similar phase separation pattern independent of the concentration. The high and low drug loads of 80- respectively 10 wt% showed a slightly larger drug concentration difference between the phase separated domains than the 50 wt% sample. No significant difference in crystallinity was detected for any of the concentrations.

Although phase separation was detected in all samples the Felodipine in ethyl cellulose dispersions were stable in its amorphous form even at drug loads as high as 80 wt% and a low crystallinity was found in all samples. Both the DSC, X-ray scattering, and tomography measurements confirmed the low crystallinity. The small part of crystallinity that was found in the samples were all detected in the drug rich phase, showing that phase separation can be an onset for crystallization.

Outlook

This study showed that ptychographic X-ray nanotomography is capable of resolving the three-dimensional nanostructure of amorphous solid dispersions and opens up for more similar measurements to be performed on amorphous solid dispersions. In future measurements it would be interesting to try to achieve a higher resolution and better signal to noise ratio by optimizing the sample preparation and utilize the optimized parameters found in this thesis. It would also be interesting to perform the same measurement for other combinations of polymers and drugs to evaluate how representative the model system of Felodipine in ethyl cellulose is.

For evaluation of how the morphology may change throughout the bulk volume it would be useful to make correlative measurements in the interior of the bulk as well as closer to the edges, specifically in the hot melt extruded samples, to detect potential differences. A scanning SAXS experiment is planned, out of the scope of this thesis, to evaluate how representative the morphology found in the interior of the sample is for the full bulk volume. The experiment will measure lower q-values corresponding to the size of the domains found in the tomograms which would make it possible to be detect the phase separation with SAXS. This can also detect possible edge effects and other possible large-scale fluctuations in the dispersion.

To gain a full understanding of the physical structure of amorphous solid dispersions it would be interesting to further extend the analysis to smaller length scales. By using high resolution methods, e.g. AFM, TEM and ssNMR, the nanostructure of the interior of the domains could be resolved and give information on how the physical structure affect the pharmaceutical performance. By correlating high resolution results with the extended volume results of the tomography a fuller understanding of the physical structure of amorphous solid dispersions could be achieved.

Further on, the effect of different morphologies on properties like stability and extended release should be evaluated to understand the effect for the pharmaceutical performance. Since it was concluded that different processing methods have an impact on the morphology it would also be interesting to look into how the processing parameters can be altered to alter the morphology. For instance, cooling rate, evaporation rate and solvent type could be examined in how it effects the nano- and microstructure of amorphous solid dispersions.

References

[1] J. Zuegg och M. A. Cooper, ”Drug-likeness and increased hydrophobicity of commercially available compound libraries for drug screening,” *Current topics in medicinal chemistry,* vol. 12, nr 14, pp. 1500-1513, 2012.

[2] S. Baghel, H. Cathcart och N. J. O'Reilly, ”Polymeric Amorphous Solid Dispersions: A Review of Amorphization, Crystallization, Stabilization, Solid-State Characterization, and Aqueous Solubilization of Biopharmaceutical Classification System Class II Drugs,” *Journal of Pharmaceutical Sciences,* vol. 105, p. 2527e2544, 2016.

[3] E. Karavas, M. Georgarakis, A. Docoslis och D. Bikiaris, ”Combining SEM, TEM, and micro-Raman techniques to differentiate between the amorphous molecular level dispersions and nanodispersions of a poorly water-soluble drug within a polymer matrix,” *International Journal of Pharmaceutics,* vol. 340, pp. 76-83, 2007.

[4] H. S. Purohit och L. S. Taylor, ”Miscibility of Itraconazole−Hydroxypropyl Methylcellulose Blends: Insights with High Resolution Analytical Methodologies,” *Molecular pharmaceutics,* vol. 12, nr 12, pp. 4542-4553, 2015.

[5] B. Tian, X. Tang och L. S. Taylor, ”Investigating the Correlation between Miscibility and Physical Stability of Amorphous Solid Dispersions Using Fluorescence-Based Techniques,” *Molecular pharmaceutics,* vol. 13, nr 11, pp. 3988-4000, 2016.

[6] H. S. Purohit, J. D. Ormes, S. Saboo, Y. Su, M. S. Lamm, A. K. P. Mann och L. S. Taylor, ”Insights into Nano- and Micron-Scale Phase Separation in Amorphous Solid Dispersions Using Fluorescence-Based Techniques in Combination with Solid State Nuclear Magnetic Resonance Spectroscopy,” *Pharmaceutical research,* vol. 34, nr 7, pp. 1364-1377, 2017.

[7] M. E. Lauer, M. Siam, J. Tardio, S. Page, J. H. Kindt och O. Grassmann, ”Rapid Assessment of Homogeneity and Stability of Amorphous Solid Dispersions by Atomic Force Microscopy—From Bench to Batch,” *Pharmaceutical Research,* vol. 30, p. 2010–2022, 2013.

[8] D. v. Drooge, W. L. J. Hinrichs, M. R. Visser och H. W. Frijlink, ”Characterization of the molecular distribution of drugs in glassy solid dispersions at the nano-meter scale, using differential scanning calorimetry and gravimetric water vapour sorption techniques,” *International Journal of Pharmaceutics,* vol. 310, nr 1-2, pp. 220-229, 2006.

[9] Y. Yoshihashi, H. Iijima, E. Yonemochi och K. Terada, ”Estimation of physical stability of amorphous solid dispersion using differential scanning calorimetry,” *Journal of Thermal Analysis and Calorimetry,* vol. 85, pp. 689-692, 2006.

[10] A. C. F. Rumondor, H. Wikström, B. V. Eerdenbrugh och L. S. Taylor, ”Understanding the Tendency of Amorphous Solid Dispersions to Undergo Amorphous–Amorphous Phase Separation in the Presence of Absorbed Moisture,” *AAPS PharmSciTech,* vol. 12, pp. 1209-1219, 2011.

[11] I. Ivanisevic, S. Bates och P. Chen, ”Novel methods for the assessment of miscibility of amorphous drug-polymer dispersions,” *Journal of Pharmaceutical Sciences,* vol. 98, nr 9, pp. 3373-3386, 2009.

[12] M. S. Nielsen, M. B. Munk, A. Diaz, E. B. L. Pedersen, M. Holler, S. Bruns, J. Risbo, K. Mortensen och R. Feidenhans’l, ”Ptychographic X-ray computed tomography of extended colloidal networks in food emulsions,” *Food structure,* vol. 7, pp. 21-28, 2016.

[13] M. Dierolf, A. Menzel, P. Thibault, P. Schneider, C. M. Kewish, R. Wepf, O. Bunk och F. Pfeiffer, ”Ptychographic X-ray computed tomography at the nanoscale,” *Nature,* vol. 467, nr 7314 , pp. 436-439, 2010.

[14] C. C. Polo, L. Pereira, P. Mazzafera, D. N. A. Flores-Borges, J. L. S. Mayer, M. Guizar-Sicairos, M. Holler, M. Barsi-Andreeta, H. W. Jr. och F. Meneau, ”Correlations between lignin content and structural robustness in plants revealed by X-ray ptychography,” *Scientific Reports,* vol. 10, p. 6023, 2020.

[15] M. Holler, A. Diaz, M. Guizar-Sicairos, P. Karvinen, E. Färm, E. Härkönen, M. Ritala, A. Menzel, J. Raabe och O. Bunk, ”X-ray ptychographic computed tomography at 16 nm isotropic 3D resolution,” *Scientific Reports,* vol. 4, p. 3857, 2015.

[16] B. C. Hancock och G. Zografi, ”Characteristics and Significance of the Amorphous State in Pharmaceutical Systems,” *Journal of pharmaceutical science,* vol. 86, nr 1, 1997.

[17] R. A. L. Jones, Soft Condensed Matter, New York: Oxford University Press, 2002.

[18] S. B. Teja, P. S. P., G. Shete, S. Patel och A. K. Bansal, ”Drug-excipient behavior in polymeric amorphous solid dispersions.,” *Journal of Excipients and Food Chemicals,* vol. 4, nr 3, p. 1048, 2016.

[19] H. S. Purohit, ”Phase Behavior of Amorphous Solid Dispersions during Hydration and Dissolution,” *Doctoral dissertation, Purdue University,* 2017.

[20] M. Maniruzzaman, J. S. Boateng, M. J. Snowden och D. Douroumis, ”A Review of Hot-Melt Extrusion: Process Technology to Pharmaceutical Products,” *ISRN Pharmaceutics,* vol. 2012, p. 436763, 2012.

[21] K. T. Savjani, A. K. Gajjar och J. K. Savjani, ”Drug solubility: importance and enhancement techniques,” *ISRN pharmaceutics,* vol. 2012, p. 195727, 2012.

[22] W. M. Groenewoud, ”Differential scanning calorimetry,” i *Characteriztion of Polymeric Materials by Thermal Analysis*, Elsevier Science BV, 2001, pp. 10-60.

[23] F. Qian, J. Huang, Q. Zhu, R. Haddadin, J. Gawel, R. Garmise och M. Hussain, ”Is a distinctive single Tg a reliable indicator for the homogeneity of amorphous solid dispersion?,” *International Journal of Pharmaceutics,* vol. 395 , p. 232–235, 2010.

[24] H. Schnablegger, The SAXS Guide, Austria: Anton Paar GmbH, vol. 4th edition, 2017 .

[25] A. Diaz, P. Trtik, M. Guizar-Sicairos, A. Menzel, P. Thibault och O. Bunk, ”Quantitative x-ray phase nanotomography,” *PHYSICAL REVIEW B,* vol. 85, nr 2, pp. 020104-1 - 020104-4, 2012.

[26] B. Lengeler, ”Coherence in X-ray physics,” *Naturwissenschaften ,* vol. 88, pp. 249-260, 2001.

[27] A. Colombo, D. E. Galli, L. D. Caro, F. Scattarella och E. Carlino, ”Facing the phase problem in Coherent Diffractive Imaging via Memetic Algorithms,” *Scientific Reports,* vol. 7, p. 42236 , 2017.

[28] M. Guizar-Sicairos, A. Diaz, M. Holler, M. S. Lucas, A. Menzel, R. A. Wepf och O. Bunk, ”Phase tomography from x-ray coherent diffractive imaging projections,” *Optics Express,* vol. 19, nr 22, pp. 21345-21357, 2011.

[29] M. Guizar-Sicairos, J. J. Boon, K. Mader, A. Diaz, A. Menzel och O. Bunk, ”Quantitative interior x-ray nanotomography by a hybrid imaging technique,” *Optica,* vol. 2, nr 3, pp. 259-266, 2015.

[30] K. Wakonig, H.-C. Stadler, M. Odstrc̆il, E. H. R. Tsai, A. Diaz, M. Holler, I. Usov, J. Raabe, A. Menzel och M. Guizar-Sicairos, ”PtychoShelves, a versatile high-level

framework for high-performance analysis of ptychographic data," *Journal of applied crystallography,* vol. 53, pp. 574-586, 2020.

[31] F. Pfeiffer, "X-ray ptychography," *Nature Photonics,* vol. 12, pp. 9-17, 2018.

[32] R. Schofield, L. King, U. Tayal, I. Castellano, J. Stirrup, F. Pontana, J. Earls och E. Nicol, "Image reconstruction: Part 1 – understanding filtered back projection, noise and image acquisition," *Journal of Cardiovascular Computed Tomography,* Available online 2019.

[33] M. Beckmann och A. Iske, "Error estimates for filtered back projection," *International Conference on Sampling Theory and Applications (SampTA) IEEE,* 2015.

[34] P. Trtik, A. Diaz, M. Guizar-Sicairos, A. Menzel och O. Bunk, "Density mapping of hardened cement paste using ptychographic X-ray computed tomography," *Cement and Concrete Composites,* vol. 36, pp. 71-77, 2013.

[35] U. D. H. Kai Briechle, "Template matching using fast normalized cross correlation," *Proceedings of SPIE, Optical Pattern Recognition XII,* vol. Vol. 4387. , pp. 95-102, 2001 .

[36] R. Sara och R. Bajcsy, "On occluding contour artifacts in stereo vision," *Proceedings of IEEE Computer Society Conference on Computer Vision and Pattern Recognition,* 1997.

[37] A. Alhalaweh, A. Alzghoul, D. Mahlin och C. A. Bergström, "Physical stability of drugs after storage above and below the glass transition temperature: Relationship to glass-forming ability," *International Journal of Pharmaceutics,* vol. 495, nr 1, pp. 312-317, 2015.

[38] K. C. Yedinak och L. M. Lopez, "Felodipine: A New Dihydropyridine Calcium-Channel Antagonist," *Annals of Pharmacotherapy,* vol. 25, nr 11, pp. 1193-1206, 1991.

[39] Ž. Knez och E. Weidner, "9.8 - Precipitation of solids with dense gases," *Industrial chemistry library,* vol. 9, pp. 587-611, 2001.

[40] U. S. Kestur och L. S. Taylor, "Evaluation of the Crystal Growth Rate of Felodipine Polymorphs in the Presence and Absence of Additives As a Function of Temperature," *Crystal growth & design,* vol. 13, nr 10, pp. 4349-4354, 2013.

[41] W. Zhang, H.-H. Zhou, Z.-Q. Liu, X.-P. Chen och Y.-J. He, "Chapter 44 - Pharmacogenomics in China," *Handbook of Pharmacogenomics and Stratified Medicine,* pp. 999-1013, 2014.

[42] S. T. Alrashood, "Chapter Three - Carbamazepine," *Profiles of Drug Substances, Excipients and Related Methodology,* vol. 41, pp. 133-321, 2016.

[43] L. W. McKeen, "14 - Renewable Resource and Biodegradable Polymers," i *Film Properties of Plastics and Elastomers*, William Andrew Publishing, 2017, pp. 449-479.

[44] M. Holler, J. Raabe, A. Diaz, M. Guizar-Sicairos, R. Wepf, M. Odstrcil, F. R. Shaik, V. Panneels, A. Menzel, B. Sarafimov, S. Maag, X. Wang, V. Thominet, H. Walther, T. Lachat, M. Vitins och O. Bunk, "OMNY—A tOMography Nano crYo stage," *Review of Scientific Instruments ,* vol. 89, p. 043706, 2018.

[45] M. v. Heel och M. Schatz, "Fourier shell correlation threshold criteria," *Journal of Structural Biology,* vol. 151, nr 3, pp. 250-262, 2005.

[46] M. Holler, J. Ihli, E. H. R. Tsai, F. Nudelman, M. Verezhak, W. D. J. v. d. Berg och S. H. Shahmoradian, "A lathe system for micrometre-sized cylindrical sample preparation at room and cryogenic temperatures," *Journal of Synchrotron Radiation,* vol. 27, pp. 472-476, 2020.

[47] M. Holler, J. Raabe, R. Wepf, S. H. Shahmoradian, A. Diaz, B. Sarafimov, T. Lachat, H. Walther och M. Vitins, "OMNY PIN—A versatile sample holder for tomographic

measurements at room and cryogenic temperatures," *Review of Scientific Instruments* , vol. 88, p. 113701, 2017.

[48] J. Schindelin, I. Arganda-Carreras, E. Frise, V. Kaynig, M. Longair, T. Pietzsch, S. Preibisch, C. Rueden, S. Saalfeld, B. Schmid, J.-Y. Tinevez, D. J. White, V. Hartenstein, K. Eliceiri, P. Tomancak och Cardona, "Fiji: an open-source platform for biological-image analysis," *Nature methods,* vol. 9, nr 7, pp. 676-682, 2012.

[49] C. T. Rueden, J. Schindelin, M. C. Hiner, B. E. DeZonia, A. E. Walter, E. T. Arena och K. W. Eliceiri, "ImageJ2: ImageJ for the next generation of scientific image data," *BMC bioinformatics,* vol. 18, nr 1, p. 529, 2017.

[50] M. Meere, G. Pontrelli och S. McGinty, "Modelling phase separation in amorphous solid dispersions," *Acta biomaterialia,* vol. 94, pp. 410-424, 2019.

[51] J. K. G. Dhont, "Spinodal Decomposition Kinetics: The Initial and Intermediate Stages," i *Dynamics: Models and Kinetic Methods for Non-equilibrium Many Body Systems*, Vol. %1 av %2. In: Karkheck J. (eds) Dynamics: Models and Kinetic Methods for Non-equilibrium Many Body Systems. NATO Science Series (Series E: Applied Sciences), vol 371. Springer, Karkheck J. NATO Science Series (Series E: Applied Sciences), vol 371. Springer, Dordrecht, 2000, pp. 73-120.

[52] F. Perrot, P. Guenoun, T. Baumberger, D. Beysens, Y. Garrabos och B. L. Neindre, "Nucleation and growth of tightly packed droplets in fluids," *Physical review letters,* vol. 73, nr 5, p. 688., 1994.

[53] S. Deshmukh, A. Paradkar, S. Abrahmsén-Alami, R. Govender, A. Viridén, F. Winge, H. Matic, J. Booth och A. Kelly, "Injection moulded controlled release amorphous solid dispersions:Synchronized drug and polymer release for robust performance," *International Journal of Pharmaceutics,* vol. 575, p. 118908, 2020.

[54] C. Luebbert, F. Huxoll och G. Sadowski, "Amorphous-Amorphous Phase Separation in API/Polymer Formulations," *Molecules,* vol. 22, nr 2, p. 296, 2017.

[55] F. P. A. Fabbiani, L. T. Byrne, J. J. McKinnon och M. A. Spackman, "Solvent inclusion in the structural voids of form II carbamazepine: single-crystal X-ray diffraction, NMR spectroscopy and Hirshfeld surface analysis," *CrystEngComm,* nr 9, pp. 728-731, 2007.

[56] C. Rustichelli, G. Gamberini, V. Ferioli, M. Gamberini, R. Ficarra och S. Tommasini, "Solid-state study of polymorphic drugs: carbamazepine," *Journal of Pharmaceutical and Biomedical Analysis,* vol. 23, nr 1, pp. 41-54, 2000.

[57] Y. Li, J. Han, G. G. Z. Zhang, D. J. W. Grant och R. Suryanarayanan, "In situ dehydration of carbamazepine dihydrate: a novel technique to prepare amorphous anhydrous carbamazepine.," *Pharmaceutical Development and Technology,* vol. 5, nr 2, pp. 257-266, 2000.

[58] H. L. Lai, K. Pitt och D. Q. Craig, "Characterisation of the thermal properties of ethylcellulose using differentialscanning and quasi-isothermal calorimetric approaches," *International Journal of Pharmaceutics,* vol. 386, pp. 178-184, 2010.

DEPARTMENT OF PHYSICS
CHALMERS UNIVERSITY OF TECHNOLOGY
Gothenburg, Sweden
www.chalmers.se

CHALMERS
UNIVERSITY OF TECHNOLOGY